

# Characterization of Silicon Carbide Biphenylene Network through $G_0W_0$ -BSE Calculations

Arushi Singh,<sup>1,\*</sup> Vikram Mahamiya,<sup>2,†</sup> and Alok Shukla<sup>1,‡</sup>

<sup>1</sup>*Department of Physics, Indian Institute of Technology Bombay, Powai, Mumbai 400076, India*

<sup>2</sup>*The Abdus Salam International Centre for Theoretical Physics (ICTP), I-34151 Trieste, Italy*

arXiv:2411.16520v1 [cond-mat.mtrl-sci] 25 Nov 2024

## Abstract

Two-dimensional silicon carbide stands out among 2D materials, primarily due to its notable band gap, unlike its carbon-based counterparts. However, the binary nature and non-layered structure of bulk SiC present challenges in fabricating its 2D counterpart. Recent advancements in technology have led to the successful synthesis of atomically thin, large-scale epitaxial monolayers of hexagonal-SiC [Polley *et al.*, Phys. Rev. Lett. 130, 076203 (2023)] and Si<sub>9</sub>C<sub>15</sub> [Gao *et al.*, Adv. Mater. 34, 2204779 (2022)], marking a significant milestone in semiconductor research. Inspired by these advancements, we have computationally designed another stable phase of 2D-SiC in the popular biphenylene network, termed SiC-biphenylene. This structure is characterized by interconnected polygons of octagons, hexagons, and tetragons arranged periodically. The dynamical and thermal stability has been confirmed through *ab initio* phonon dispersion and molecular dynamics simulations. The structure demonstrates a high melting point of approximately 3475 K and a “direct” band gap of 2.16 eV using the HSE06 functional. Upon considering many-body effects, the quasiparticle band gap widens to 2.89 eV at the G<sub>0</sub>W<sub>0</sub> level, indicating pronounced electron correlation effects within the material. Our analysis further reveals that the effective mass of charge carriers exhibits higher values along the  $\Gamma \rightarrow Y$  compared to the  $\Gamma \rightarrow X$  direction. Moreover, the optical spectrum obtained from solving the Bethe-Salpeter equation (G<sub>0</sub>W<sub>0</sub>+BSE) identifies the first optically active exciton peak at 2.07 eV, corresponding to a strongly bound exciton with a binding energy of 0.82 eV. The effective mass and Bohr radius of the exciton are calculated to be 1.01  $m_0$  and 2.14 Å, respectively, demonstrating the characteristic of a Frenkel exciton. Furthermore, the investigation into stable bilayer structures across various stacking configurations (AA, AA', and AB-stacked) highlights the impact of stacking patterns on excitonic binding energies, with AA-stacked configuration indicating the presence of Mott-Wannier exciton. Our investigation extends to identifying the stable bulk phase of SiC-biphenylene, revealing lower self-energy corrections compared to monolayer and bilayer structures, attributed to increased electron delocalization in bulk structures.

---

\* arushi.phy@iitb.ac.in

† vmahamiy@ictp.it

‡ shukla@iitb.ac.in

## I. INTRODUCTION

The diverse hybridization ( $sp$ ,  $sp^2$ ,  $sp^3$ ) schemes of the valence electronic orbitals of the carbon atom lead to an extensive array of one- (1D), two- (2D), and three- (3D) dimensional allotropic forms of carbon, with controllable physicochemical properties and potential application in various fields. A few carbon phases, including fullerene [38], graphene [64], graphdiyne [44], phagraphene [84], naphyne [47], graphtetrayne [66], have been successfully synthesized in laboratory experiments. Numerous carbon allotropes such as, pentaheptite [11], haeckelites [79], graphenylene [75], pentahexoctite [73],  $\Psi$ -graphene [46], graphyne [45], tetra-graphene [4], D-graphyne [88], P-graphyne [88], etc., have been identified theoretically. Hence, an extensive experimental and theoretical investigations have been conducted on carbon nanomaterials. To date, the SACADA database [29] currently catalogs around 500 different carbon allotropes, highlighting the extensive diversity present within the carbon family and its significance in the field of materials science.

In 2010, Hudspeth *et al.* [31] theoretically predicted a novel fully  $sp^2$  bonded planar carbon allotrope known as the biphenylene network, which consists of the periodically connected octagon- ( $o$ ), hexagon- ( $h$ ), and square- ( $s$ ) rings. The carbon atoms in the biphenylene network are three-fold coordinated, thereby maintaining the same number of neighbors as in the hexagonal network of graphene structure. However, the associated  $sp^2$  bonds of carbon atoms undergo deformation, transitioning to a purely metallic state in biphenylene [3]. The non-benzoid octagonal rings of biphenylene facilitate enhanced lithium-ion and sodium-ion storage capacity compared to graphene, thus positioning it as a promising candidate for application as an anode material [10, 15, 24]. A first-principles investigation by Liu *et al.* [51] revealed that the carbon atoms in the tetragonal rings of biphenylene are substantially positively charged, rendering them viable active sites for the oxygen reduction reaction (ORR). The rotational vibration phonon mode of the six-membered carbon ring exhibits strong coupling with electrons, leading to the possibility of superconductivity with a predicted critical temperature of 6.2 K [17]. This critical temperature can further be enhanced to 27.4 K and 21.5 K by applying small uniaxial strain and impurity doping, respectively. The biphenylene structure can also generate quasi-1D nanotubes and nanoribbons exhibiting diverse edge geometries compared to graphene [13]. In a recent breakthrough, Fan *et al.* [14] successfully fabricated the ultra-flat biphenylene nanoribbons on Au(111) surface through an interpoly-

mer dehydrofluorination (HF-zipping) reaction. Scanning probe microscopy (SPM) analysis was conducted to investigate the influence of nanoribbon widths on their band gaps. It was established that metallicity emerges with increasing nanoribbon width, thus affirming the metallic properties of the biphenylene sheet, consistent with previous theoretical prediction [3, 31, 53]. This marks a significant milestone in the experimental realization of a nanostructure composed of non-benzoid rings and their distinct characteristics.

Two-dimensional silicon carbide (2D-SiC) monolayers represent a novel category of semi-conducting monolayers, distinguished by their exceptional properties. While the theoretical concept of a two-dimensional allotrope of SiC has been under discussion for an extended period, its experimental synthesis has remained elusive owing to the non-layered structure of bulk SiC. Unlike graphene, the bulk structure of SiC cannot serve as a parent structure for the mechanical exfoliation to create 2D materials. However, recent progress in synthesis methodologies has introduced a novel approach for generating these non-layered 2D-structures through epitaxial growth on appropriate substrates. Very recently, Polley et al. [69] reported the large-scale synthesis of an epitaxial monolayer of honeycomb SiC through the annealing of thin films of transition metal carbides grown on 4H-SiC(0001) substrate. This newly synthesized 2D phase of SiC exhibits a planar structure and possesses a wide band gap of 2.5 eV. It demonstrates excellent stability at high temperatures, up to 1200 °C in a vacuum environment. Another significant milestone in 2D-SiC research is the recent achievement by Gao and co-workers [16], who synthesized large-scale atomic monolayer Si<sub>9</sub>C<sub>15</sub> on Ru(0001) and Rh(111) substrates. This synthesis involves growing a graphene layer on a Ru or Rh substrate, followed by silicon evaporation onto the graphene surface and high-temperature annealing to form the Si<sub>9</sub>C<sub>15</sub> layer. The resulting monolayer Si<sub>9</sub>C<sub>15</sub> exhibits robust environmental stability and features a buckled honeycomb structure with a bandgap of  $\approx 1.9$  eV.

Inspired by the recent experimental synthesis of 2D-SiC allotropes, namely hexagonal SiC [69] and Si<sub>9</sub>C<sub>15</sub> [16], alongside the established synthesis of the biphenylene network utilizing carbon atoms [14], in this work we have computationally designed the silicon carbide counterpart within the biphenylene network, referred to as SiC-biphenylene. Several novel materials have been foreseen through computational modeling, which emphasize the crucial contribution of theoretical predictions in advancing the development of novel materials. In recent investigations involving both computational predictions and laboratory synthesis, a

variety of 2D silicon carbide (SiC) materials have surfaced that share structural topology with carbon-based monolayers [52, 82, 85, 89]. SiC-based monolayers exhibit a wide band gap with high thermal and mechanical stability, making them useful for high-power electronic devices with distinct on/off switching behavior [32, 48, 74, 77]. The recent experimental fabrication of a 2D biphenylene network of carbon atoms and 2D-SiC monolayer strongly suggest the potential realization of the SiC-biphenylene structure in the near future.

The remainder of this paper is structured as follows. The subsequent Sec. II outlines the computational details and theoretical methods, including descriptions of the ground-state, quasiparticle, and electron-hole interaction calculations. In Sec. III A, we present a comprehensive analysis of the dynamical, thermal, and mechanical stability of the novel SiC-biphenylene monolayer structure. Sec. III B explores the electronic and excitonic properties in detail, while Sec. III C investigates the mechanical strength and elasticity of the structure. In Sec. III D, we discuss the results of finite-temperature molecular dynamics simulations of the monolayer over a wide temperature range. Additionally, in Sec. III E, we explore the stability of SiC-biphenylene in various bilayer stacking configurations and its bulk structure, providing a comprehensive summary of the material’s transition from monolayer to bilayer to and finally to the bulk forms in Sec. IV.

## II. METHOD

We performed the first principles calculations using density functional theory (DFT) employing the VASP simulation package [35–37]. Electron-ion interactions were described using the projector-augmented plane wave (PAW) approximation [7]. Electronic wave functions were expanded using a plane wave basis set with a kinetic energy cutoff of 520 eV. Monkhorst-Pack k-point grid of  $9 \times 9 \times 1$  has been employed to sample the Brillouin zone [58]. Additionally, a vacuum space of 20 Å was maintained along the z-direction to prevent interactions between periodic images of the monolayer. The energy and force convergence limit is set to be  $10^{-7}$  eV and  $10^{-3}$  eV Å<sup>-1</sup>, respectively. The structural relaxations and the ground state energies were calculated using the generalized gradient approximation (GGA) within the Perdew–Burke–Ernzerhof (PBE) parametrization [67]. It is widely recognized that the GGA functional tends to underestimate the band gap, while the Hartree-Fock (HF) method overestimates it [40]. Therefore, to get a more accurate prediction of band gap [5],

we employed screened hybrid-functional HSE06 [26–28], which is constructed by mixing 25% of Fock exchange ( $E_x^{HF}$ ) with 75 % of PBE exchange ( $E_x^{PBE}$ ) in the short range. Thus, the exchange–correlation energy is calculated as:

$$E_{xc}^{HSE06} = \frac{1}{4}E_x^{HF,SR}(\omega) + \frac{3}{4}E_x^{PBE,SR}(\omega) + E_x^{PBE,LR}(\omega) + E_c^{PBE}, \quad (1)$$

where  $E_x^{HF,SR}$  and  $E_x^{PBE,SR}$  denote the short-range components of Hartree-Fock and PBE exchange energies, respectively.  $E_x^{PBE,LR}$  is the long-range PBE exchange energy, and  $E_c^{PBE}$  is the PBE correlation energy.  $\omega = 0.11 \text{ bohr}^{-1}$  serves as the screening parameter [39].

The lattice dynamical stability is verified by evaluating the phonon dispersion using the Density Functional Perturbation Theory (DFPT) approach. For this evaluation, we employed a  $9 \times 9 \times 1$  Monkhorst-Pack k-point grid for the monolayer structure and a  $5 \times 5 \times 1$  Monkhorst-Pack k-point grid for both the bilayer and bulk structures. These grids were selected to ensure adequate sampling of the Brillouin zone while balancing computational cost and accuracy. The PHONOPY [80] software is employed to determine the requisite force constants essential for calculating the phonon spectra. The thermal stability at finite temperature is tested by employing ab-initio molecular dynamics (AIMD) simulations [62]. First, the system is kept in a microcanonical ensemble (NVE) for 6 ps with 1 fs time steps while raising the temperature to a desired value. Then, the system is equilibrated in a canonical ensemble (NVT) for 6 ps at that temperature, utilizing a Nose–Hoover thermostat [63].

In analyzing the energetics, the cohesive energy ( $E_C$ ) and formation energy ( $\Delta E_F$ ) of the monolayer system have been calculated using the following expressions :

$$E_C = \frac{E_T^{biphenylene-SiC} - (N_{Si}E_T^{Si} + N_C E_T^C)}{N_{Si} + N_C}, \quad (2)$$

$$\Delta E_F = \frac{\mu^{biphenylene-SiC} - (N_{Si}\mu^{Si} + N_C\mu^C)}{N_{Si} + N_C} \quad (3)$$

where  $E_T^{biphenylene-SiC}$  represents the total energy of the SiC-biphenylene unit cell,  $E_T^{SiC}$  and  $E_T^C$  denote the total energies of isolated Si and C atoms, respectively.  $\mu^{biphenylene-SiC}$  stands for the chemical potential of the SiC-biphenylene unit cell;  $\mu^{Si}$  and  $\mu^C$  represent the chemical potentials of the stable bulk phases of Si and C atoms, respectively.  $N_{Si}$  and  $N_C$  refer to the number of Si and C atoms in a monolayer unit cell, respectively.

To model the interlayer interactions in bilayer systems, we employed the semi-empirical DFT-D3 method developed by Grimme [22, 23]. In this approach, van der Waals interactions are incorporated by adding a semi-empirical dispersion potential to the conventional DFT energy framework. This dispersion potential is parameterized using empirical fit parameters derived from a range of reference systems. To more accurately capture long-range van der Waals (vdW) forces, we also employed non-local vdW functionals, namely optB86b-vdW [33] and optB88-vdW [34]. These functionals account for vdW interactions directly within the exchange-correlation functional, rather than relying on an empirical correction. The inter-layer binding energy  $E_{ib}$  is then calculated using the expression :

$$E_{ib} = \frac{E_T^{bilayer-biphenylene-SiC} - 2E_T^{biphenylene-SiC}}{N_{Si} + N_C}, \quad (4)$$

where  $E_T^{bilayer-biphenylene-SiC}$  and  $E_T^{biphenylene-SiC}$  represent the total energies of the bilayer and monolayer systems, respectively, calculated using the DFT-D3 corrections.  $N_{Si}$  and  $N_C$  denote the number of Si and C atoms, respectively, in a bilayer unit cell.

While the DFT approach has demonstrated remarkable efficacy in characterizing the ground-state properties of materials, its ability to adequately describe excited-state phenomena, such as optical properties, in 2D systems is quite limited due to the strong excitonic effects inherent to these materials. Therefore, we employed many-body perturbation theory (MBPT) approaches to accurately calculate and understand the many-electron properties of these systems [18, 76]. We computed the quasi-particle (QP) band structure using single shot  $G_0W_0$  approximation [65], utilizing the eigenvalues and eigenstates from HSE06 as input to determine the QP energies. This method approximates the quasi-particle (QP) self-energy as the product of the Green's function  $G$  and the dynamically screened Coulomb interaction  $W$ , serving as a first-order perturbation correction to the Kohn-Sham eigenvalues. In practice, QP energies are derived as

$$E_{n\mathbf{k}}^{qp} = \epsilon_{n\mathbf{k}} + Z_{n\mathbf{k}}[\Sigma_{n\mathbf{k}}(G, W; \epsilon_{n\mathbf{k}}) - v_{n\mathbf{k}}^{xc}] \quad (5)$$

where  $\epsilon_{n\mathbf{k}}$  represents the Kohn-Sham eigenvalues.  $\Sigma_{n\mathbf{k}}(\omega)$  and  $v_{n\mathbf{k}}^{xc}$  denote the expectation values of the self-energy and the exchange-correlation potential, respectively, over the  $n\mathbf{k}$  Kohn-Sham eigenvector.  $Z_{n\mathbf{k}}$  signifies the quasiparticle (QP) renormalization factor, which is defined as

$$Z_{n\mathbf{k}} = \left[ 1 - \frac{\partial \Sigma_{n\mathbf{k}}(\omega)}{\partial \omega} \Big|_{\omega=\epsilon_{n\mathbf{k}}} \right]^{-1} \quad (6)$$

This approach allows the calculation of the quasiparticle shifts for all electronic states and at all considered  $\mathbf{k}$  points. We employed 160 empty conduction band and  $7 \times 7 \times 1$  k-mesh grid to conduct the  $G_0W_0$  calculations. Subsequently, the QP band structure was interpolated using the maximally localized Wannier functions (MLWFs) [56] implemented in the WANNIER90 package [60].

The excitonic optical properties, which incorporate electron-hole interactions, were investigated by solving the Bethe-Salpeter equation (BSE) [42, 70] built upon  $G_0W_0$  eigenvalues and wave functions. The excitation energy  $\Omega^S$  and the corresponding exciton amplitude  $A_{v\mathbf{c}\mathbf{k}}^S$  of the correlated electron-hole excitations are determined by solving the following BSE equation

$$(E_{c\mathbf{k}} - E_{v\mathbf{k}})A_{v\mathbf{c}\mathbf{k}}^S + \sum_{v'\mathbf{c}'\mathbf{k}'} \langle v\mathbf{c}\mathbf{k} | K^{eh} | v'\mathbf{c}'\mathbf{k}' \rangle A_{v'\mathbf{c}'\mathbf{k}'}^S = \Omega^S A_{v\mathbf{c}\mathbf{k}}^S \quad (7)$$

Here,  $E_{c\mathbf{k}}$  and  $E_{v\mathbf{k}}$  are the  $G_0W_0$  eigenvalues of conduction and valence bands, respectively, at a specific  $\mathbf{k}$  point.  $K^{eh}$  is the kernel describing the screened interaction between excited electrons and holes. The excitonic eigenstates were constructed based on the 48 highest valence bands and the 24 lowest conduction bands.

The Bohr radius  $a^{exciton}$  of a ground state exciton with a corresponding binding energy  $E_b^{exciton}$  can be calculated using the following equation [19, 71, 72]

$$a^{exciton} = \frac{\varepsilon_r}{\mu^{exciton}} \times a_h \times m_0 \quad (8)$$

Here,  $m_0$  represents the rest mass of the electron,  $\varepsilon_r$  denotes the dielectric constant,  $a_h$  stands for the Bohr radius (0.529Å),  $R_h$  signifies the Rydberg constant (13.6 eV). The effective mass of the exciton, denoted by  $\mu^{exciton}$ , is determined as  $\mu^{exciton} = \frac{E_b^{exciton}}{R_h} \times \varepsilon_r^2 \times m_0$ .

The mechanical properties were calculated by subjecting the equilibrium structure to strains ranging from -2% to +2% in increments of 0.05%. The elastic energy  $\Delta E(V, \{\varepsilon_i\})$  of a material under strain is expressed using Voigt notation [1] and can be described in the



following harmonic approximation:

$$\Delta E(V, \{\varepsilon_i\}) = E(V, \{\varepsilon_i\}) - E(V_0, 0) = \frac{V_0}{2} \sum_{i,j=1}^6 C_{ij} \varepsilon_i \varepsilon_j \quad (9)$$

where  $E(V, \{\varepsilon_i\})$  and  $E(V_0, 0)$  are the total energies of the strained and unstrained lattice, with the volumes of  $V$  and  $V_0$ , respectively. Thus, the elastic tensor ( $C_{ij}$ ) is derived from the second-order derivative of the total energies versus strain. The orientation-dependent Young's Modulus  $E(\theta)$  and the Poisson's ratio  $\nu(\theta)$  can then further be obtained using the following equations :

$$E(\theta) = \frac{C_{11}C_{22} - C_{12}^2}{C_{11} \sin^4(\theta) + A \sin^2(\theta) \cos^2(\theta) + C_{22} \cos^4(\theta)}, \quad (10)$$

$$\nu(\theta) = \frac{C_{12} \sin^4(\theta) - B \sin^2(\theta) \cos^2(\theta) + C_{12} \cos^4(\theta)}{C_{11} \sin^4(\theta) + A \sin^2(\theta) \cos^2(\theta) + C_{22} \cos^4(\theta)} \quad (11)$$

where  $A = \frac{C_{11}C_{22} - C_{12}^2}{C_{66}} - 2C_{12}$  and  $B = \frac{C_{11}C_{22} - C_{12}^2}{C_{66}} - 2C_{12}$ .

### III. RESULTS AND ANALYSIS

#### A. Structural conformation and experimental feasibility

This section presents the atomic arrangement and structural properties of an optimized ground state geometry of SiC-biphenylene monolayer (Fig.1). The lattice belongs to the Pmma space group and possesses an orthorhombic crystal structure. The regular primitive cell, composed of 6-Si-atoms and 6-C-atoms, consists of two fused octagons (enclosed by black dashed lines in Fig.1a) with lattice vectors  $\vec{a}$  and  $\vec{b}$  of magnitudes 5.61 Å and 9.44 Å, respectively. The  $b/a$  ratio is 1.68, which corresponds to structural anisotropy along x- and y-direction, giving rise to direction-dependent electronic, mechanical and, optical properties, which we shall discuss later in Sec.III B & III C. The planar structure of SiC-biphenylene monolayer consists of eight-, six-, and four-membered polygons of connected octagon, hexagon and tetragon. As illustrated in Fig.(1a), the structure consists of two types of atomic sites corresponding to Si (namely, Si<sub>1</sub> and Si<sub>2</sub>) and C (namely, C<sub>1</sub> and C<sub>2</sub>) atoms, respectively, where atoms Si<sub>1</sub> and C<sub>1</sub> are shared by the two adjacent octagons and one hexagon, while atoms Si<sub>2</sub> and C<sub>2</sub> are shared by an adjacent octagon, hexagon

and tetragon. This configuration results in four different bond lengths:  $\overline{Si_1C_1} = 1.80 \text{ \AA}$ ,  $\overline{Si_2C_1} = 1.78 \text{ \AA}$ ,  $\overline{Si_2C_2} = 1.79 \text{ \AA}$  ( $1.82 \text{ \AA}$ ),  $\overline{Si_1C_2} = 1.77 \text{ \AA}$ , as shown in Fig.(1a). The Bader charge analysis also confirmed that the two types of atomic sites ( i.e. ( $Si_1, C_1$ ) and ( $Si_2, C_2$ ) ) correspond to different effective charges, and hence exhibit different contribution to the energy bands (Fig.2b & c) and the site-dependent chemical activity against the foreign atom. To validate our DFT schemes employed, we optimized the geometry of a recently synthesized novel biphenylene carbon sheet, and the lattice vectors are calculated to be  $4.52 \text{ \AA}$  and  $3.76 \text{ \AA}$ , which match precisely with previous theoretical reports [3, 54, 68, 83, 87]. Further, to reveal the bonding character between the constituent atoms, the Electron Localization Function (ELF) is computed (Fig.1b), and the values are renormalized between 0 (completely delocalized electrons) to 1 (completely localized electrons). A highly pronounced localized electron density is found between Si and C atoms, indicating the strong covalent-type character of the bond between them. A small amount of delocalized electrons around the C-atom is observed, which is attributed to its higher electronegativity than the Si-atom, leading to the slight deformation of the octagon and tetragon rings as compared to the biphenylene structure composed of all carbon atoms.

Next, we addressed the experimental feasibility of the freestanding monolayer of SiC-biphenylene based on cohesive energy, formation energy, phonon spectrum, ab-initio molecular dynamics (AIMD) simulations, and elastic constants. The computed cohesive energy  $E_C$  of SiC-biphenylene is  $-5.72 \text{ eV/atom}$  which is lower than that of biphenylene ( $-7.40 \text{ eV/atom}$ )[55] but comparable to those of biphenylene-MoS<sub>2</sub>( $-4.94 \text{ eV/atom}$ ) [20] and SiC monolayer ( $-5.93 \text{ eV/atom}$ ) [6, 74], demonstrating the structural stability of the the system. The formation energy  $\Delta E_F$  is found to be  $0.52 \text{ eV/atom}$ , which is close to the formation energy of experimentally synthesized materials, such as SiC monolayer ( $0.29 \text{ eV/atom}$ ) [25, 74] and biphenylene ( $0.46 \text{ eV}$ ) (see Table I), which suggests that the monolayer structure of SiC-biphenylene is energetically stable. Further, we computed the elastic constants which satisfy the Born–Huang criteria [8]  $C_{11}C_{22} - C_{12}^2 > 0$  and  $C_{66} > 0$  showcasing the mechanical stability of the newly designed monolayer system (detailed results are discussed in Sec.III C). To evaluate the lattice dynamical stability at 0 K, phonon dispersion calculations were conducted (Fig.1c). The highest optical phonon mode reaches a frequency of  $1206.41 \text{ cm}^{-1}$ . The three acoustic phonon modes exhibit slight imaginary frequencies near the  $\Gamma$ -point, which, in all likelihood, are numerical artifacts. These artifacts typically arise

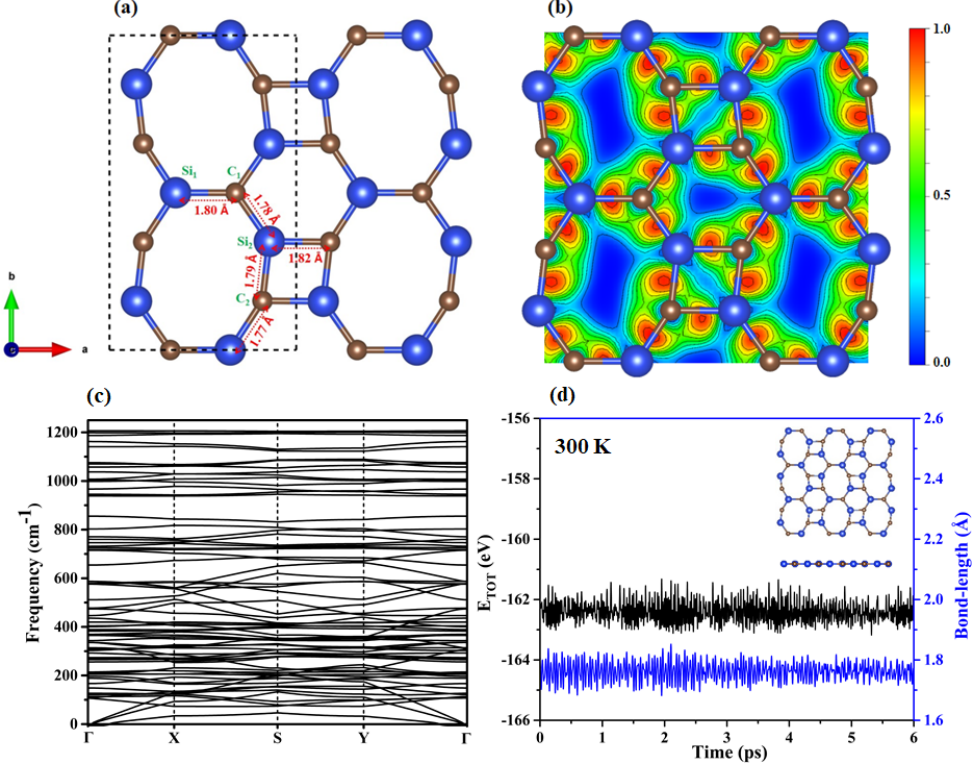


Figure 1. (a) Optimized atomic structure of 2D SiC-biphenylene monolayer. The unit cell is delineated by black dashed lines. Two distinct atomic sites are represented by  $(Si_1, C_1)$  and  $(Si_2, C_2)$ ; (b) Contour line diagrams of the ELF electronic distributions; (c) Calculated phonon modes with all real frequencies along the high symmetry directions of Brillouin zone; (d) Fluctuations in total energy and bond length at 300 K for 6 ps with the steps of 1 fs (inset shows the optimised structure at 300 K)

from limitations in the computational method, such as the use of finite-size supercells or insufficient convergence settings, particularly affecting long-wavelength (low-energy) acoustic phonons, and have been frequently reported in the literature [50, 61]. The absence of large imaginary frequencies in the overall phonon dispersion confirms the dynamic stability of the structure at 0 K. Additionally, the material's response to the thermal perturbations at room temperature (300 K) was also assessed by employing *ab-initio* Molecular Dynamics (AIMD) Simulations. The total energy exhibited a maximum fluctuation of 1.08 eV, indicating a stable thermal response (Fig.1d). Furthermore, bond length fluctuations were analyzed, with the  $\overline{Si_2C_1}$  bond showing a variation of  $0.09 \text{ \AA}$  (Fig.1d). Across the monolayer, which contains four different types of bond lengths, the fluctuations ranged from  $0.07 \text{ \AA}$  to  $0.12 \text{ \AA}$ .

These small variations in bond lengths suggest that the system retains structural integrity under thermal perturbation, confirming its thermodynamic stability at the room temperature. The snapshot of the final stage of AIMD simulation (inset of Fig.1d), demonstrates that the structure is stable without any bond-reconstruction. Thus, our simulation results collectively suggest the excellent structural, thermal, and mechanical stability of the newly predicted SiC-biphenylene monolayer system.

Material	Lattice Constants (Å)	Formation Energy $\Delta E_F$ (eV/atom)	Cohesive Energy $E_C$ (eV/atom)	Band Gap $E_g^{HSE06} / E_g^{G_0W_0}$ (eV)
SiC-biphenylene	5.61, 9.44	0.52	-5.72	2.16 / 2.89
Biphenylene [54, 55]	4.52, 3.76	0.46	-7.40	Metallic
h-SiC [2, 6, 74]	3.09, 3.09	0.29	-5.94	3.38 / 3.96

Table I. Calculated values of lattice constants, formation energy ( $\Delta E_F$ ), cohesive energy ( $E_C$ ) and band gap ( $E_g^{HSE06} / E_g^{G_0W_0}$ ) for 2D SiC-biphenylene monolayer. Corresponding values of 2D Biphenylene and h-SiC monolayers have also been included for the sake of comparison.

### B. Electronic and excitonic properties

The electronic band structure of a monolayer of SiC-biphenylene has been investigated using HSE06 and  $G_0W_0$  methodologies, as depicted in Fig. 2a. In this figure, the blue dotted line represents the band structure obtained from HSE06, while the black line corresponds to the band structure derived from  $G_0W_0$  calculations. The SiC-biphenylene monolayer exhibits a “direct” band gap of 2.16 eV at the HSE06 level, with the Valence Band Maximum (VBM) and Conduction Band Minimum (CBM) located at the high-symmetry point  $\Gamma$  of the Brillouin zone. Upon considering many-body effects, the Quasiparticle (QP) band gap increases to 2.89 eV at the  $G_0W_0$  level, indicating a self-energy correction of 0.73 eV. This substantial quasiparticle correction arises from the enhanced  $e - e$  interactions and reduced screening in lower dimensions. Though HSE06 incorporates non-local exchange effects, it

results in a smaller gap compared to the  $G_0W_0$  method. This underscores the significant influence of the Coulomb screening effect, which is predominantly captured by the self-energy operator in the  $G_0W_0$  scheme, on the electronic structure of monolayer SiC-biphenylene. However, the general shape and nature of band gap remain consistent across both HSE06 and  $G_0W_0$  methodologies.

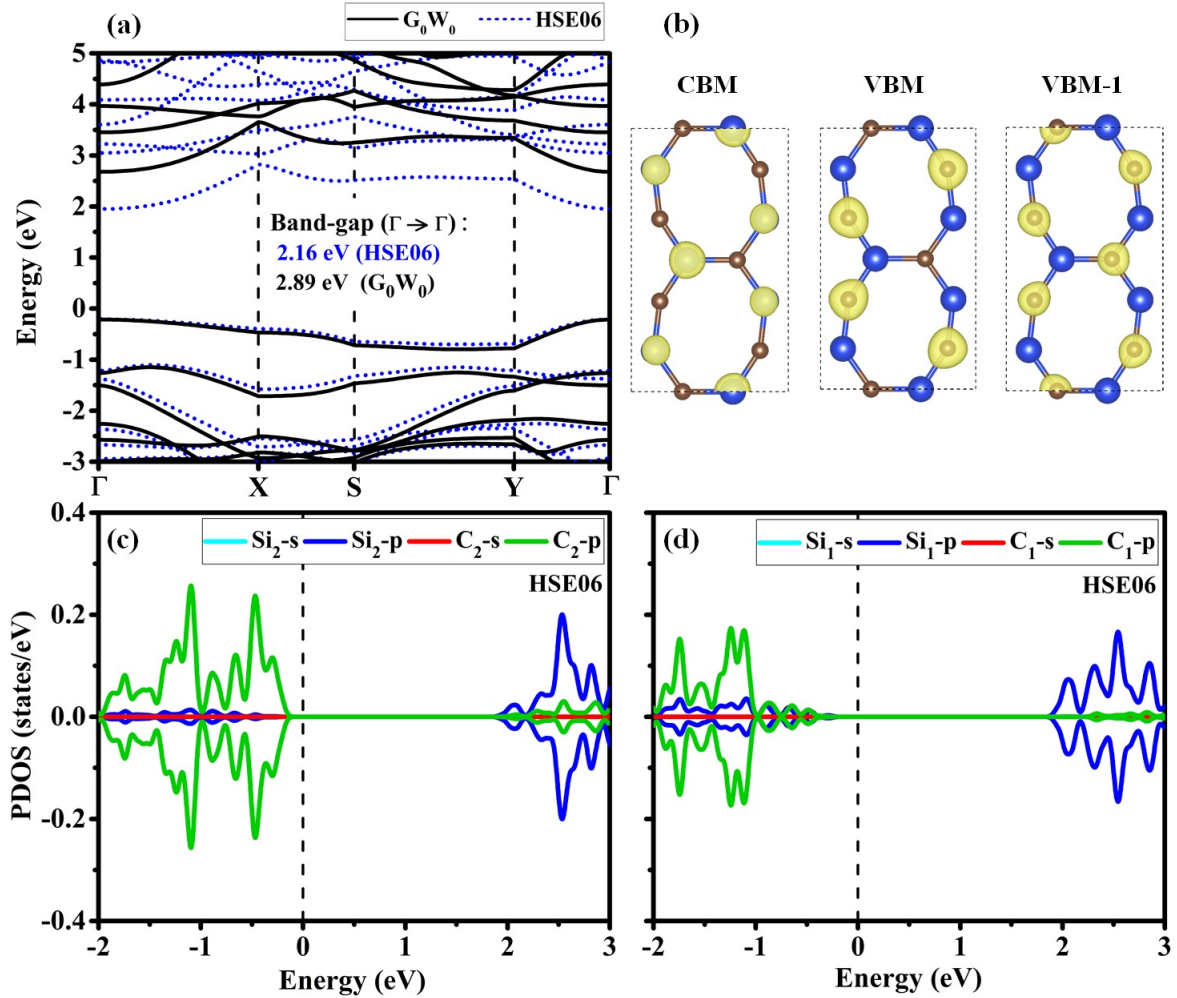


Figure 2. (a) Electronic energy band structure at HSE06 (blue dotted line) and  $G_0W_0$  (black solid line) levels of theory; (b) Partial charge density plot for the lower conduction band (CBM) and the upper two valence bands (VBM and VBM-1); (c) & (d) Projected density of states (PDOS) of a 2D SiC-biphenylene monolayer. Zero of the energy is set to  $E_F$ .

Fig. 2b displays the partial charge density of the Conduction Band Minimum (CBM) and two uppermost Valence Bands (i.e., VBM & VBM-1). The primary contribution to the VBM charge density comes from electrons distributed around the  $C_2$  type atoms, while electrons

from both  $C_1$  and  $C_2$  atoms contribute to the VBM-1. This inference is further supported by PDOS (Fig. 2c-d), which indicates that the  $C_2$  atoms dominate the valence band edge compared to the  $C_1$  atoms. Similarly, in the conduction band, the contribution of the  $Si_1$  atoms surpasses that of the  $Si_2$  atoms. This highlights the site-specific chemical reactivity characteristic of the Si and C atoms. The valence band edge primarily comprises the p-orbitals of the carbon atoms, while the p-orbital of the Si atom primarily contributes to the conduction band edge. As the band edges comprise different atoms, this property facilitates the separation of charge carriers and extends the lifetime of excitons, suggesting potential applications as a photoactive layer in solar cells. Additionally, the symmetric nature of the PDOS for spin-up and spin-down channels confirms the non-magnetic nature of this material. Therefore, we employed non spin-polarized calculations for further exploration.

The mobility and behavior of charge carriers in semiconductors are heavily influenced by the effective masses of electrons and holes, which determine their usefulness in optoelectronic devices. Notably, there exists an anisotropy in the effective masses of electrons and holes around the Conduction Band Minimum (CBM) and Valence Band Maximum (VBM) respectively. The electron effective mass is estimated to be  $0.25 m_0$  and  $1.34 m_0$  along  $\Gamma \rightarrow Y$  and  $\Gamma \rightarrow X$  directions, respectively. While the effective mass of holes is determined to be  $0.28 m_0$  and  $2.21 m_0$  along  $\Gamma \rightarrow Y$  and  $\Gamma \rightarrow X$  directions, respectively. Consequently, the charge carriers will demonstrate higher mobility along the  $\Gamma \rightarrow Y$  direction in comparison to the  $\Gamma \rightarrow X$  direction.

Moving from single-electron properties (i.e., electronic levels) to two-particle properties, such as optical absorption, an additional step in the many-body description is necessary. This involves accounting for the Coulombic interactions between excited electrons in the conduction band and holes generated in the valence band, resulting in the formation of a bound pair of electron and hole, i.e., an exciton. These excitonic effects are crucial for understanding the optical properties of 2D-materials [12, 86]. To incorporate these excitonic effects, the Bethe-Salpeter equation (BSE) is solved on top of  $G_0W_0$  corrected energies. While performing  $G_0W_0$  calculations, we selected orbitals from HSE06 as the starting point, a critical factor for accurately estimating optical properties.

Due to the significant depolarization effect in 2D materials for light polarization perpendicular to the surface, the optical spectrum for  $E||z$  polarization is negligible. Consequently, our analysis will concentrate exclusively on the in-plane polarizations (i.e.,  $E||xx$

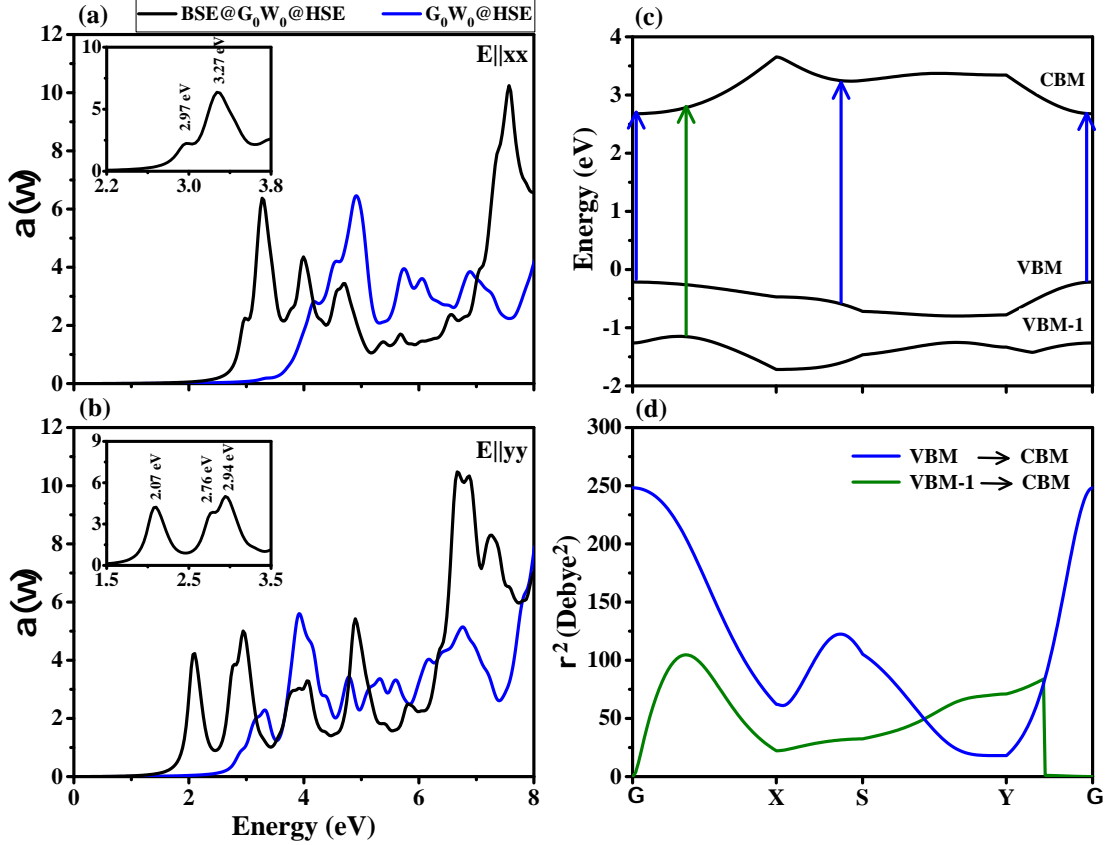


Figure 3. (a) & (b) correspond to the excitonic absorption spectrum for light polarized along the x-direction (E||xx) and y-direction (E||yy), obtained using different levels of theory:  $G_0W_0@HSE$  (blue solid line) and  $BSE@G_0W_0@HSE$  (black solid line). (c) Electronic band structure, and (d) Transition dipole moment (TDM) for the 2D SiC-biphenylene monolayer. The allowed dipole transitions are shown with colored arrows.

and E||yy). In Fig. (3a-b), we compare the optical absorption spectra of monolayer SiC-biphenylene computed at two levels of theory: one with the inclusion of electron-hole interaction ( $BSE@G_0W_0@HSE$ ), and the other without electron-hole interaction ( $G_0W_0@HSE$ ). The introduction of electron-hole interaction results in a red-shift in the optical spectra with strongly bound exciton states below the  $G_0W_0$  band gap (2.89 eV), which are notably absent in the  $G_0W_0@HSE$  spectrum. As illustrated in Fig. (3a-b), the absorption spectra for light polarization along the x and y axes (i.e., E||xx and E||yy) differ significantly, with the absorption edge blue-shifted for E||xx. This strong effect of light polarization on the absorption spectra is primarily due to the anisotropic structure of the material along the x and y directions. In anisotropic materials, the structural arrangement, such as the orientation

of atoms and bonds, varies along different crystallographic axes. This structural anisotropy influences how the material interacts with polarized light, as the interaction depends on the alignment of the material’s structure relative to the polarization direction of the light. Consequently, light polarized along the x or y axis interacts differently with the material, resulting in distinct absorption characteristics at specific energies.

We identified two optically active (bright) excitons at 2.07 eV and 2.76 eV, both of which lie below the  $G_0W_0$  band gap of 2.89 eV and are formed by light polarized in the y-direction. The calculated binding energy of the first exciton, located at 2.07 eV, is determined to be 0.82 eV. Although this value is lower than the theoretically predicted binding energies for h-SiC (1.11 eV) [30] and Si<sub>9</sub>C<sub>15</sub> (1.14 eV) [78], it remains significantly higher than the predicted exciton binding energy for bulk 2H-SiC, which is 0.1 eV [30]. These findings suggest that excitons in 2D materials experience strong confinement due to reduced dimensionality, which enhances the overlap of electron and hole wave functions and results in pronounced excitonic effects. The calculated Bohr radius and effective mass of the first exciton, generated by y-polarized light, are 2.14 Å and 1.01  $m_0$ , respectively. Notably, the Bohr radius is smaller than the lattice parameters ( $|\vec{a}| = 5.61$  Å,  $|\vec{b}| = 9.44$  Å), further indicating the strong confinement of the exciton within the unit cell. This is a characteristic of the Frenkel exciton [57]. In addition to the bright excitons generated by y-polarized light, we identified the first bright exciton generated by x-polarized light at 2.97 eV. This highlights the anisotropic nature of the optical response of excitons within the 2D SiC-biphenylene monolayer, driven by the interplay between the reduced dimensionality and the inherent anisotropy in the crystal lattice. Apart from optically active (bright) excitons, there are many optically inactive (dark) excitons. However, we find no dark excitons below the first bright exciton, corroborating the “direct” band gap nature of monolayer SiC-biphenylene. Notably, a cluster of three dark excitons with nearly identical energies appears just below the second bright exciton at 2.76 eV.

Next, we calculated the transition probabilities from the valence band maximum (VBM) to the conduction band minimum (CBM), as shown in Fig. (3c-d). The highest magnitude of the transition dipole moment (TDM) for the VBM to CBM transition occurs at the  $\Gamma$ -point. In contrast, the TDM is minimum at the X and Y points for this transition, indicating that optical absorption is forbidden at these points. For the transition between VBM-1 and CBM, the transition probability is highest between the  $\Gamma$  and X points in the Brillouin zone.



### C. Elastic properties

Gaining insights into the mechanical properties of a material is essential for its effective utilization in device manufacturing. Strain engineering is one of the prevalent strategies for tailoring the properties of nanomaterials. Strains can occur due to the mismatch of lattice constants with the substrate. Hence, a comprehensive knowledge of mechanical properties is highly desirable. The full reversible lattice response to the small strain around equilibrium is quantified by the elastic modulus. To determine the elastic constants, we applied a series of strains ranging from -2% to +2% with a step size of 0.05%, assessing the total energy of the material at each interval. Subsequently, by fitting the energy-strain curves using Eqn.9, we obtained the elastic constants:  $C_{11} = 118.66$ ,  $C_{12} = 61.66$ ,  $C_{22} = 171.00$ , and  $C_{66} = 43.56$ , respectively. The elastic constants clearly satisfy the Born–Huang criteria [8]  $C_{11}C_{22} - C_{12}^2 > 0$  and  $C_{66} > 0$ , indicating the mechanical stability of the material. To estimate the mechanical strength, the direction-dependent Young’s Modulus  $E(\theta)$  and Poisson’s Ratio  $\nu(\theta)$  are calculated based on the calculated elastic constants using Eqns.10 & 11. The calculated Young’s Modulus  $E(\theta)$  of SiC-biphenylene along x ( $\sim 0^\circ$ ) and y ( $\sim 90^\circ$ ) directions is 96.44 N/m and 138.97 N/m, respectively, implying the mechanical anisotropy of the system, as shown in Fig. (4a). The values are notably lower than those of biphenylene and graphene structures (Table II), likely due to the larger lattice constant and lower symmetry of SiC-biphenylene relative to Biphenylene and graphene. The corresponding Poisson’s ratio along x ( $\sim 0^\circ$ ) and y ( $\sim 90^\circ$ ) directions are 0.36 and 0.52, respectively (4b). The positive Poisson’s ratio indicates that when a compressive (tensile) strain is applied in one direction, SiC-biphenylene tends to expand (contract) in the perpendicular direction [21]. The relatively low Young’s modulus of SiC-biphenylene offers the potential to utilize it in flexible electronics and to tailor its mechanical properties through strain engineering.

### D. Melting Point

We conducted a comprehensive analysis of the thermal stability and melting behavior of SiC-biphenylene using *ab-initio* Molecular Dynamics (MD) simulations across a temperature range varying from 300 K to 4500 K. Fig.5a represents the variation of total energy with respect to temperature. The total energy increases linearly from 300 K to 3460 K, followed

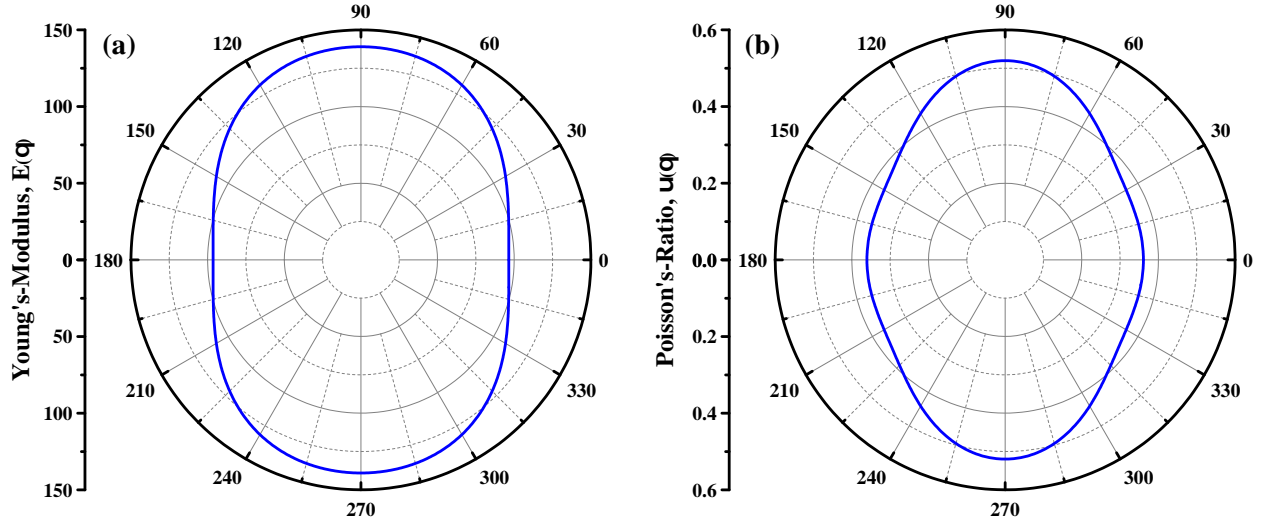


Figure 4. Calculated orientation dependent (a) Young's Modulus  $E(\theta)$ , and (b) Poisson's Ratio  $\nu(\theta)$  of a 2D SiC-biphenylene monolayer

Material	Young's Modulus (N/m)		Poisson's Ratio	
	$E_x$	$E_y$	$\nu_x$	$\nu_y$
SiC-biphenylene	96.44	138.97	0.36	0.52
Biphenylene [55]	212.4	259.7	0.31	0.38
h-SiC [32]	166	166	0.29	0.29
Graphene [9, 32]	335	335	0.16	0.16

Table II. Calculated values of Young's Modulus ( $E_x, E_y$ ) and Poisson's Ratio ( $\nu_x, \nu_y$ ) for 2D SiC-biphenylene monolayer. Corresponding values of 2D Biphenylene and h-SiC monolayers have also been included for the sake of comparison.

by an abrupt jump within the range of 3460 K to 3520 K. This sudden surge in total energy is attributed to increased atomic kinetic energy driven by the intense lattice thermal vibrations, marking the onset of the melting process between 3460 K and 3520 K. During this temperature interval, we monitored corresponding changes in structural morphology. At 3460 K, the structure retains its integrity, experiencing bond deformation without any bond breakage. However, the structure is highly strained due to robust thermal fluctuations at the elevated temperature. Beyond 3475 K, the lattice thermal vibrations intensify significantly,

resulting in the rupture of Si-C bonds (Fig.5c), initiating the melting process. Consequently, SiC-biphenylene exhibits a high melting point comparable to that of hexagonal-SiC (4050 K) [43], graphene (4095 K) [81] and biphenylene (4024 K) [68]. By 3500 K, the structure transitions into entangled and interconnected chains of Si and C atoms, forming a quasi-2D liquid state. Subsequently, at 3600 K (Fig.5f), clustering of Si and C atoms occurs, ultimately leading to the complete dissociation of the material.

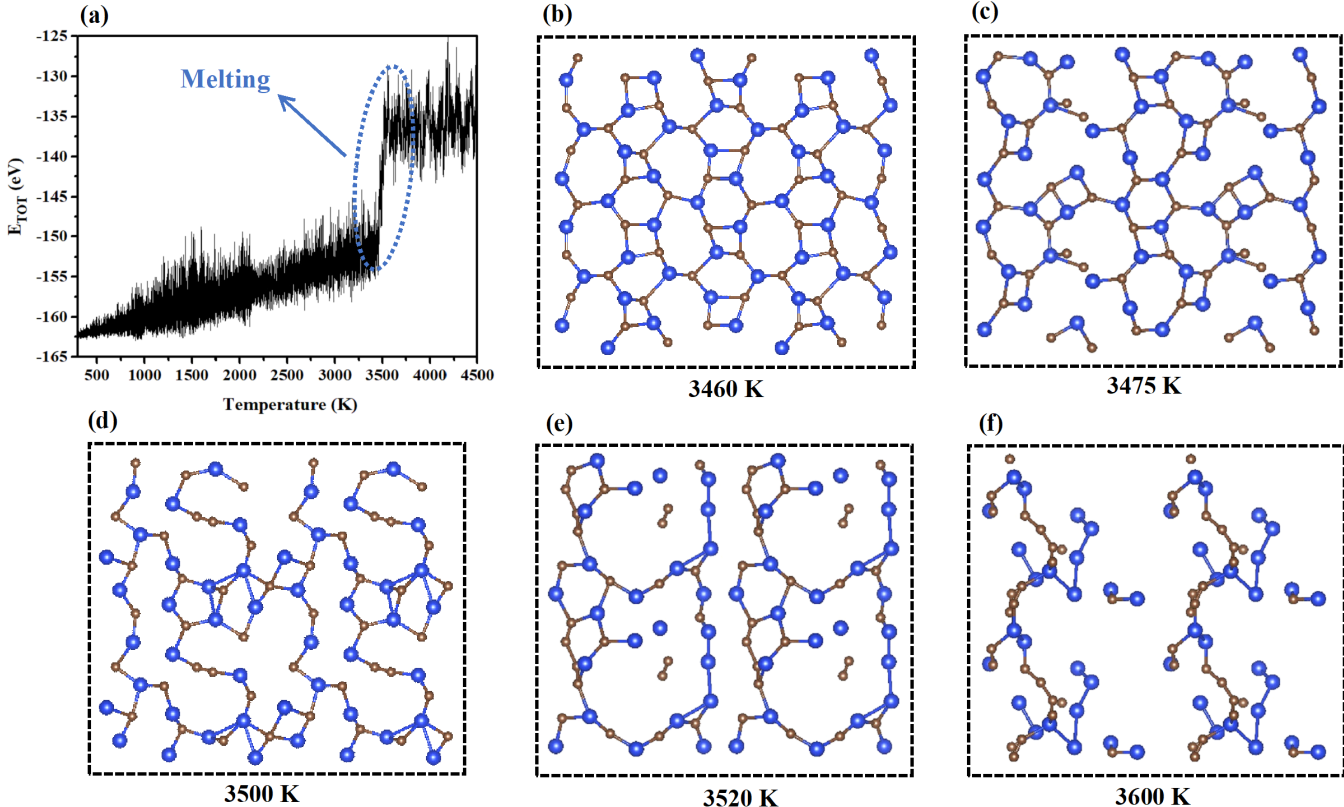


Figure 5. (a) Variation of total energy  $E_{TOT}$ (eV) with temperature ranging from 300 K to 4500 K for 2D SiC-biphenylene monolayer. A sudden jump in  $E_{TOT}$ (eV) is seen between 3460 K and 3520 K. MD snapshots of structure at (b) 3460 K , (c) 3475 K, (d) 3500 K, (e) 3520 K, and (c) 3600 K. Bond breakage is observed at 3475 K, signifying the onset of the melting process.

### E. Bilayer and bulk structures

We constructed the bilayers of SiC-biphenylene by stacking the two monolayers of SiC-biphenylene in various stacking configurations: AA-stacked (where the top layer is aligned

over the bottom layer with zero translation,  $\tau_x = 0$ ); AA'-stacked (where the top layer is offset from the bottom layer with a translation,  $\tau_x = \frac{a}{3}$ ); and AB-stacked (where the Si and C atoms are interchanged, i.e., the Si atoms of the top layer align with the C atoms of the bottom layer, and vice versa). These configurations are depicted in Fig. (6). To evaluate the interlayer binding energies in bilayer stackings, we initially employed the semi-empirical DFT-D3 method to account for van der Waals (vdW) interactions. For the AA-stacked bilayer, the computed interlayer binding energy is -22.5 meV/atom, which is comparable to that of the biphenylene bilayer (-22.0 meV/atom) [13, 59]. This suggests that the AA-stacked layers are predominantly stabilized by weak van der Waals interactions, maintaining a planar geometry with an interlayer distance of 4.23 Å. In contrast, the interlayer binding energies for the AA'- and AB-stacked bilayers are significantly higher, at -110.8 meV/atom and -173.7 meV/atom, respectively, suggesting the possibility of weak vertical bond formation in addition to van der Waals interactions. We further observe a buckling of 0.72 and 0.64 Å in AA'- and AB-stacked geometries, respectively (refer to Fig. 6). In order to capture vdW interactions more effectively, we extended our analysis by employing non-local vdW functionals, specifically vdW-opt-b86b and vdW-opt-b88. The results reveal that the non-local functionals predict stronger binding energies across all stackings compared to DFT-D3 (Table IV), reflecting their ability to capture long-range vdW interactions more effectively. Notably, the non-local vdW potentials predict even stronger binding in AA'- and AB-stacked configurations as compared to AA-stacked configuration. Although the binding energies differ between methods, the bond lengths remain nearly identical, suggesting that the equilibrium geometries are largely unaffected by the choice of vdW corrections. We observed that the buckling in the AA'-stacked bilayer structure can be eliminated through the intercalation of noble gases such as Ar, Kr, and Xe, resulting in interlayer distances of 6.63 Å, 6.92 Å, and 7.35 Å, respectively. The very recent experimental investigations of the encapsulation of noble gas atoms such as krypton (Kr), (Xe) and alkali metal atoms within bilayer graphene have opened new avenues for research on encapsulated two-dimensional van der Waals solids, with potential applications in quantum information technology and energy storage [41, 49].

Fig. (7a, c, and e) illustrates the phonon band dispersion for AA, AA', and AB-stacked bilayer systems, respectively. The absence of imaginary vibration frequencies across the Brillouin zone confirms the dynamic stability of these stacking configurations. To confirm

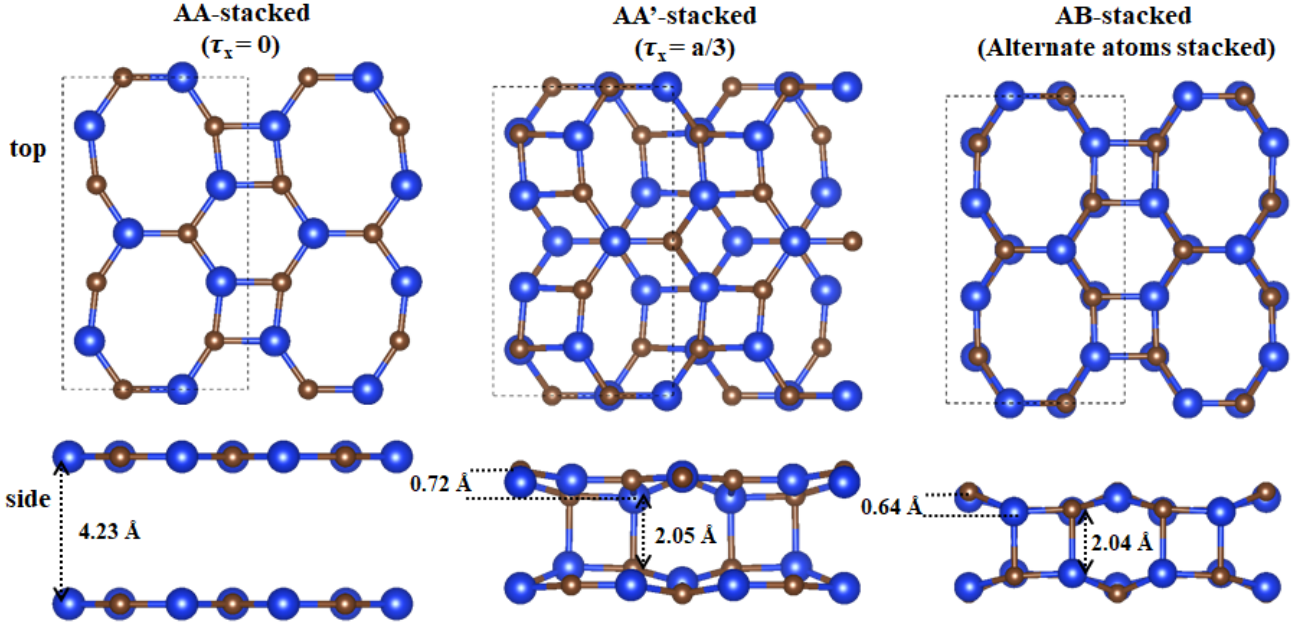


Figure 6. Optimised atomic structure of SiC-biphenylene bilayer with different stacking patterns : AA-stacked, AA'-stacked and AB-stacked. The interlayer distance and buckling height have been marked in the figure.

their thermal stability at room temperature (300 K), AIMD simulations were conducted, revealing that the structural integrity is preserved. For the AA, AA', and AB-stacked bilayer systems, the total energy fluctuations are approximately 2.42 eV ( $\sim 0.74\%$ ), 2.60 eV ( $\sim 0.80\%$ ), and 2.37 eV ( $\sim 0.72\%$ ), respectively, with  $\overline{Si_2C_1}$  bond length fluctuations of 0.07 Å, 0.12 Å, and 0.12 Å for each corresponding stacking configuration. Fluctuations in other bond lengths are observed within a similar range, from 0.06 Å to 0.16 Å. Furthermore, to evaluate their mechanical stability, the equilibrium systems were strained by small amounts (-2% to +2%) to determine the elastic constants. The derived elastic constants satisfy the Born-Huang criteria[8]  $C_{11}C_{22} - C_{12}^2 > 0$  and  $C_{66} > 0$ , confirming the thermal stability of AA, AA', and AB-stacked bilayer systems.

To further investigate the influence of bilayer interactions across various stacking configurations, we conducted band structure computations employing HSE06 and  $G_0W_0$  methodologies. The band gap and quasi-particle (QP) self-energy corrections undergo significant variations for different stacking patterns (III). It is evident from Fig. (8a) that the electronic characteristic of AA-stacked bilayer resembles their constituent monolayers with a relative shift in energy attributed to the weak van der Waals interactions. The band gap narrows to

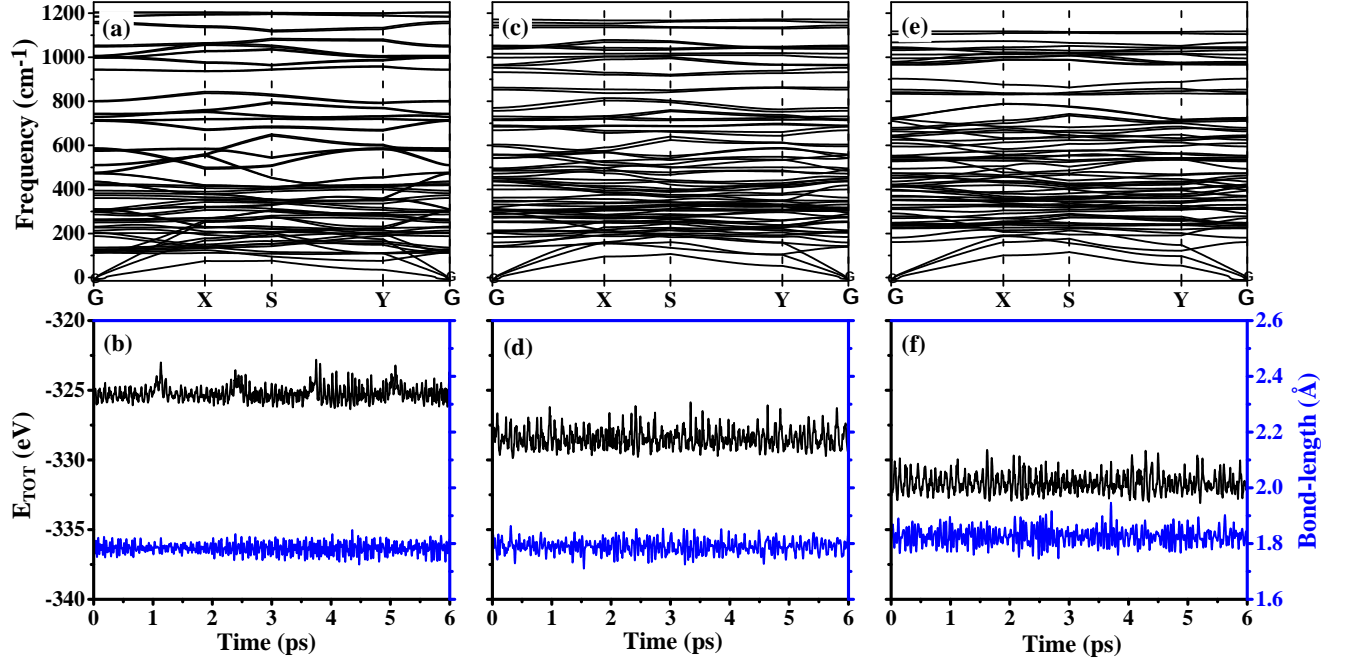


Figure 7. (a), (c), and (e) illustrate the calculated phonon dispersion along high symmetry directions for AA, AA', and AB stacked bilayers. In (b), (d), and (f), the variation in total energy and bond lengths at 300 K is depicted for AA, AA', and AB stacked bilayers, respectively.

2.06 eV ( $G_0W_0$ ); however, nature remains “direct” at the  $\Gamma$ -point of the Brillouin zone. In contrast, the electronic structure of AA'- and AB-stacked bilayers significantly differs from their constituent monolayers due to the vertical chemical interaction between the layers, in addition to van der Waals interactions. This interaction results in reduction of interlayer spacing and the formation of vertical bonds. Additionally, the atoms within the bilayers arrange themselves into hexagonal and tetragonal rings due to the formation of vertical bonds (Fig.6). The band gap transitions to an “indirect” nature and increases to 3.04 eV (with the valence band maximum (VBM) at Y and the conduction band minimum (CBM) at  $\Gamma$ ) for AA'-stacked bilayers, and to 3.43 eV (with the VBM at  $\Gamma$  and the CBM at X) for AB-stacked bilayers, as shown in Fig. (8d-g). It is evident that for the bilayers, both the nature and the magnitude of the band gap strongly depend on the stacking order.

In Table III, we present the estimated effective masses of electrons (holes) in the direction from CBM (VBM) to the nearest high-symmetry point in the Brillouin Zone. Consistent with the band structure calculations, the effective masses exhibit directional dependence due to the anisotropy of the energy dispersion curves. Specifically, in the AA-stacked configu-

SiC- biphenylene	$E_g(\text{HSE06})$ (eV)	$E_g^{QP}(\text{G}_0\text{W}_0)$ (eV)	$m_e$ ( $m_0$ )	$m_h$ ( $m_0$ )	$E_1^{exciton}$ (eV)	$E_b^{exciton}$ (eV)	$\mu^{exciton}$ ( $m_0$ )	$a^{exciton}$ (Å)
monolayer	2.16 (Direct)	2.89 (Direct)	1.34 ( $\Gamma \rightarrow X$ ) 0.25 ( $\Gamma \rightarrow Y$ )	2.21 ( $\Gamma \rightarrow X$ ) 0.28 ( $\Gamma \rightarrow Y$ )	2.07 (E  yy)	0.82	1.01	2.14
AA-stacked bilayer	1.54 (Direct)	2.06 (Direct)	1.57 ( $\Gamma \rightarrow X$ ) 0.21 ( $\Gamma \rightarrow Y$ )	2.90 ( $\Gamma \rightarrow X$ ) 0.32 ( $\Gamma \rightarrow Y$ )	1.89 (E  yy)	0.17	0.16	11.80
AA'-stacked bilayer	2.31 (Indirect)	3.04 (Indirect)	2.04 ( $\Gamma \rightarrow X$ ) 0.34 ( $\Gamma \rightarrow Y$ )	0.95 ( $Y \rightarrow S$ ) 0.87 ( $Y \rightarrow \Gamma$ )	2.52 (E  yy)	0.64	0.55	3.28
AB-stacked bilayer	2.57 (Indirect)	3.43 (Indirect)	0.05 ( $X \rightarrow \Gamma$ ) 0.47 ( $X \rightarrow S$ )	0.44 ( $\Gamma \rightarrow X$ ) 2.18 ( $\Gamma \rightarrow Y$ )	3.06 (E  xx)	0.64	0.44	3.69
bulk (ABA...- stacked)	2.78 (Direct)	3.01 (Direct)	1.30 ( $\Gamma \rightarrow X$ ) 0.18 ( $\Gamma \rightarrow Y$ )	0.45 ( $\Gamma \rightarrow X$ ) 0.89 ( $\Gamma \rightarrow Y$ )	3.21 (E  xx)	0.20	0.31	7.88

Table III. Band gaps calculated using HSE06 ( $E_g$ ) and  $\text{G}_0\text{W}_0(E_g^{QP})$ . The electron ( $m_e$ ) and hole ( $m_h$ ) effective masses calculated along the direction of their band extrema. First excitonic energy ( $E_1^{exciton}$ ) and its corresponding binding energy ( $E_b^{exciton}$ ), effective mass ( $\mu^{exciton}$ ), and Bohr radius ( $a^{exciton}$ ) are listed for the monolayer, bilayer, and bulk systems.

ration, the effective mass of electrons and holes along the  $\Gamma \rightarrow Y$  direction demonstrates an approximately 88% reduction compared to that along the  $\Gamma \rightarrow X$  direction. Notably, the effective mass of electrons is 0.054 for  $X \rightarrow \Gamma$  in the AB-stacked bilayer, suggesting that carriers behave more like free particles with high mobility. This characteristic is advantageous for semiconductor applications requiring fast charge transport and efficient device performance.

To explore the influence of stacking patterns on excitonic effects, we analyze the optical properties of bilayer configurations with varying stacking arrangements. Notable distinctions emerge among the absorption spectra across these varied configurations. The first bright excitonic peak is observed at 1.89 eV (E||yy) for AA-stacked configurations, 2.52 (E||yy) eV for AA'-stacked, and 3.06 eV (E||xx) for AB-stacked configurations, with the corresponding binding energies of 0.17 eV, 0.64 eV, and 0.64 eV, respectively (Table III). Distinct excitonic behaviors are evident across these stacking configurations, with AA-stacked configurations

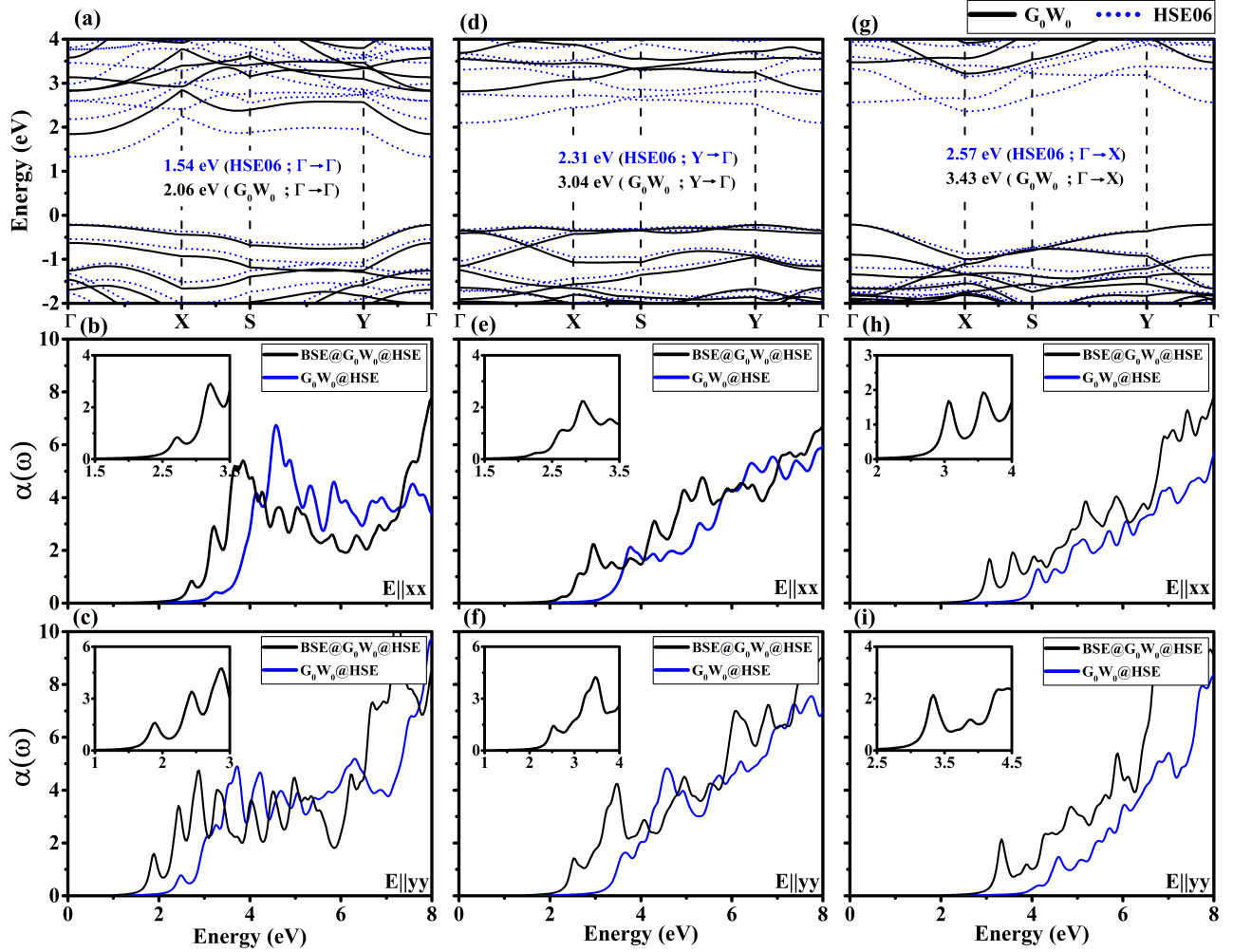


Figure 8. (a), (d), and (g) show electronic band structures for AA, AA', and AB stacked bilayers at HSE06 (blue dotted line) and  $G_0W_0$  (black solid line) levels of theory, with  $E_F$  set at zero. (b) and (c) depict excitonic optical spectra for AA-stacked structures. (e) and (f) represent excitonic optical spectra for AA'-stacked structures. (h) and (i) illustrate excitonic optical spectra for AB-stacked structures, calculated using  $G_0W_0$ @HSE (blue solid line) and BSE@ $G_0W_0$ @HSE (black solid line)

exhibiting the presence of Mott-Wannier excitons. In contrast, excitons in AA'-stacked and AB-stacked configurations are significantly more localized compared to those in the AA-stacked bilayer.

Furthermore, we examined the mechanical strength of AA, AA', and AB-stacked bilayer systems by computing the direction-dependent Young's Modulus and Poisson's ratio (Fig. 9). Young's Modulus values increase (indicating higher stiffness) for bilayer stackings, with the highest observed for AA-stacked bilayers. Clearly, the number of layers and atomic



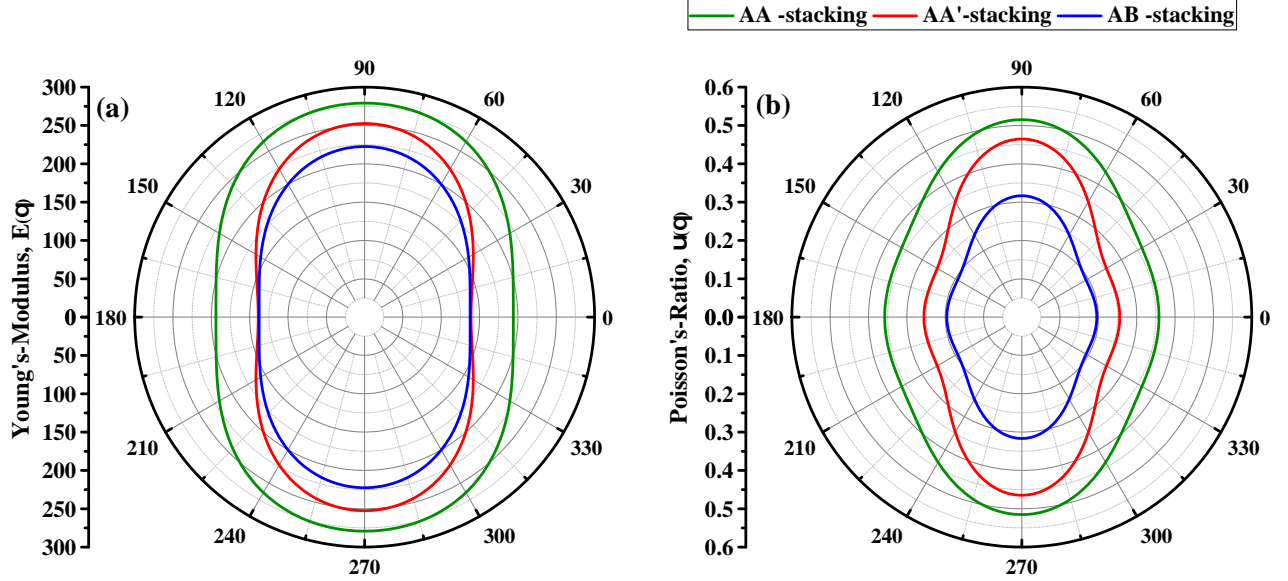


Figure 9. Calculated orientation dependent (a) Young's Modulus  $E(\theta)$  and (b) Poisson's Ratio  $\nu(\theta)$  for AA, AA', and AB stacked bilayers.

stacking significantly affect the material's stiffness. The minimum and maximum values of Young's Modulus are observed along the x and y directions, respectively, similar to the monolayer case of SiC-biphenylene (Table IV). The Poisson's ratio for AA-stacked bilayers remains the same as that obtained for monolayers, which can be attributed to weak van der Waals interactions between the layers. However, for AA' and AB-stacked bilayers, weak vertical bonds are formed, which largely reduce the property of lateral contraction upon extension, resulting in lower Poisson's values compared to monolayer SiC-biphenylene.

Among the three bilayer stacking geometries, the AB geometry exhibits the highest binding energy, estimated at around -173.7 meV/atom, indicating superior stability for the formation of bulk structures. Consequently, we opt for an AB stacking configuration when constructing the bulk structure of SiC-biphenylene. The absence of imaginary frequencies (Fig.10c) confirms dynamical stability at 0 K. Furthermore, thermal stability analysis conducted through AMID calculations demonstrates that bulk-SiC-biphenylene maintains its stability at room temperature. The vertical chemical bonds are reinforced, providing a robust interlayer binding energy of -395 meV/atom. The structure exhibits isotropy along the xy and yz planes, featuring rings of octagons, hexagons, and tetragons (Fig.10a). In contrast, along the xz-plane, only octagon and tetragon rings are observed (Fig.10b). The quasi-particle band gap is calculated to be 3.01 eV, with a self-energy correction of 0.23 eV

Stacking-type	Young's Modulus (N/m)		Poisson's Ratio		Interlayer binding energy (meV/atom)		
	$E_x$	$E_y$	$\nu_x$	$\nu_y$	DFT-D3	optB86b-vdW	optB88-vdW
AA-stacked	193.90	279.15	0.36	0.51	-22.5	-32.08	-32.92
AA'-stacked	138.77	252.49	0.25	0.46	-110.83	-142.08	-121.25
AB-stacked	137.56	222.52	0.19	0.32	-173.75	-208.75	-171.67

Table IV. Calculated values of Young's Modulus ( $E_x, E_y$ ) and Poisson's Ratio ( $\nu_x, \nu_y$ ) for different bilayer stackings. The interlayer binding energies were also computed using semi-empirical DFT-D3 and non-local vdW functionals (vdW-opt-b86b and vdW-opt-b88).

to the HSE06 value (Fig.10d). The lower magnitude of the self-energy correction compared to monolayer and bilayer systems can be attributed to the dimensionality effect, where electrons are more delocalized in the bulk, thus reducing the impact of electron-electron correlation. Bulk SiC-biphenylene exhibits its first excitonic peak at 3.21 eV ( $E||xx$ ) with a binding energy of 0.20 eV (Fig.10e). The corresponding Bohr radius of the exciton is 7.88 Å, indicating that this peak corresponds to a Mott-Wannier exciton. As the material transitions from monolayer to bulk, excitonic optical absorptions become less significant.

#### IV. CONCLUSION

In this article, we have computationally designed a stable novel SiC allotrope within a biphenylene network, comprising interconnected polygons of octagons, hexagons, and tetragons arranged in a periodic fashion. The structure exhibits excellent thermal stability, with a high melting point of 3475 K. Computational analysis of its mechanical properties indicates that SiC-biphenylene is softer compared to graphene and biphenylene, making it suitable for high-power flexible electronic devices. Our findings indicate that it is a "direct" band gap semiconductor with a quasiparticle (QP) band gap value of 2.89 eV ( $G_0W_0$ ). The atom-projected Density of States (DOS) reveals that the Conduction Band Minimum (CBM) and Valence Band Maximum (VBM) are composed of the p-orbitals of Si and C atoms, re-

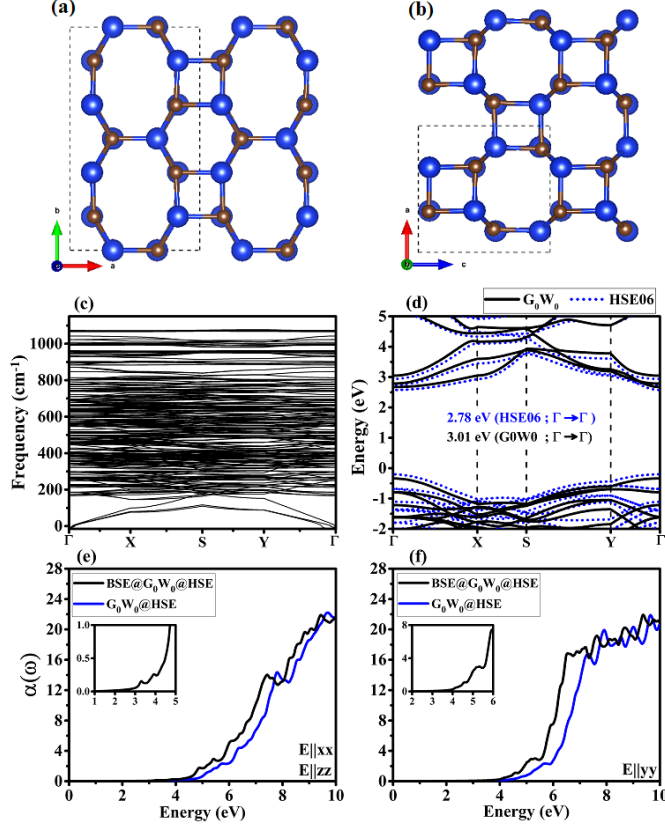


Figure 10. Optimised structure of bulk-SiC-biphenylene (stacked in ABAB... configuration) projected on (a) xy-plane, (b) xz-plane, (c) calculated phonon dispersion, (d) electronic band structure along the high symmetry directions of Brillouin zone, and (e) & (f) optical absorption spectrum calculated using  $G_0W_0@HSE$  (blue solid line) and  $BSE@G_0W_0@HSE$  (black solid line)

spectively, which may facilitate exciton separation in photovoltaic applications. Moreover, the effective mass of charge carriers along the  $\Gamma \rightarrow Y$  direction is found to be less than that along the  $\Gamma \rightarrow X$  direction, suggesting enhanced mobility along the former path. Additionally, a sharp excitonic peak below the QP band gap indicates the presence of a strongly bound bright exciton with a binding energy of 0.82 eV. Furthermore, the anisotropic optical excitations over a wide spectral range result in polarization-dependent optical properties.

Our investigation extended to include bilayer structures formed in three distinct stacking geometries (AA, AA', and AB-stacked), analyzing their energetics, stability, as well as electronic and optical properties. We found that both the nature and magnitude of band gap depends on stacking order of bilayer structure. Additionally, we explored the influence of stacking patterns on excitonic effects and observed notable distinctions in the absorption

spectra. Specifically, excitons are found to be more localized in AA' and AB-stacked configurations compared to the AA-stacked configuration. Furthermore, by examining specific stacking configurations, we have identified the bulk structure of SiC-biphenylene (ABAB...-stacked) and confirmed its characteristic “direct” band gap. As the material transitions from monolayer to bulk, excitonic optical absorptions become less significant. In summary, our study offers in-depth insights into the electronic and optical characteristics of monolayer SiC-biphenylene, as well as its bilayer and bulk configurations. We anticipate that the results presented in this paper will broaden the understanding of the properties of 2D SiC nanomaterial allotropes.

- 
- [1] R. C. Andrew, R. E. Mapasha, A. M. Ukpog, and N. Chetty. Mechanical properties of graphene and boronitrene. *Phys. Rev. B*, 85:125428, Mar 2012.
- [2] C. Attaccalite, A. Nguer, E. Cannuccia, and M. Grüning. Strong second harmonic generation in sic, zno, gan two-dimensional hexagonal crystals from first-principles many-body calculations. *Phys. Chem. Chem. Phys.*, 17:9533–9540, 2015.
- [3] A Bafekry, M Faraji, MM Fadlallah, HR Jappor, S Karbasizadeh, M Ghergherehchi, and D Gogova. Biphenylene monolayer as a two-dimensional nonbenzenoid carbon allotrope: a first-principles study. *Journal of Physics: Condensed Matter*, 34(1):015001, 2021.
- [4] Arka Bandyopadhyay and Debnarayan Jana. A review on role of tetra-rings in graphene systems and their possible applications. *Reports on Progress in Physics*, 83(5):056501, 2020.
- [5] Veronica Barone, Oded Hod, Juan E. Peralta, and Gustavo E. Scuseria. Accurate prediction of the electronic properties of low-dimensional graphene derivatives using a screened hybrid density functional. *Accounts of Chemical Research*, 44(4):269–279, Apr 2011.
- [6] E. Bekaroglu, M. Topsakal, S. Cahangirov, and S. Ciraci. First-principles study of defects and adatoms in silicon carbide honeycomb structures. *Phys. Rev. B*, 81:075433, Feb 2010.
- [7] P. E. Blöchl. Projector augmented-wave method. *Phys. Rev. B*, 50:17953–17979, Dec 1994.
- [8] Max Born, Kun Huang, and M Lax. Dynamical theory of crystal lattices. *American Journal of Physics*, 23(7):474–474, 1955.
- [9] Emiliano Cadelano, Pier Luca Palla, Stefano Giordano, and Luciano Colombo. Elastic properties of hydrogenated graphene. *Phys. Rev. B*, 82:235414, Dec 2010.
- [10] Xin-Wei Chen, Zheng-Zhe Lin, and Xi-Mei Li. Biphenylene network as sodium ion battery anode material. *Phys. Chem. Chem. Phys.*, 25:4340–4348, 2023.
- [11] Vincent H Crespi, Lorin X Benedict, Marvin L Cohen, and Steven G Louie. Prediction of a pure-carbon planar covalent metal. *Physical Review B*, 53(20):R13303, 1996.
- [12] Pierluigi Cudazzo, Claudio Attaccalite, Ilya V. Tokatly, and Angel Rubio. Strong charge-transfer excitonic effects and the bose-einstein exciton condensate in graphane. *Phys. Rev. Lett.*, 104:226804, Jun 2010.
- [13] Salih Demirci, Şafak Çallıoğlu, Taylan Görkan, Ethem Aktürk, and Salim Ciraci. Stability and electronic properties of monolayer and multilayer structures of group-iv elements and

- compounds of complementary groups in biphenylene network. *Phys. Rev. B*, 105:035408, Jan 2022.
- [14] Qitang Fan, Linghao Yan, Matthias W Tripp, Ondřej Krejčí, Stavrina Dimosthenous, Stefan R Kachel, Mengyi Chen, Adam S Foster, Ulrich Koert, Peter Liljeroth, et al. Biphenylene network: A nonbenzenoid carbon allotrope. *Science*, 372(6544):852–856, 2021.
- [15] David Ferguson, Debra J Searles, and Marlies Hankel. Biphenylene and phagraphene as lithium ion battery anode materials. *ACS applied materials & interfaces*, 9(24):20577–20584, 2017.
- [16] Zhao-Yan Gao, Wenpeng Xu, Yixuan Gao, Roger Guzman, Hui Guo, Xueyan Wang, Qi Zheng, Zhili Zhu, Yu-Yang Zhang, Xiao Lin, Qing Huan, Geng Li, Lizhi Zhang, Wu Zhou, and Hong-Jun Gao. Experimental realization of atomic monolayer si9c15. *Advanced Materials*, 34(35):2204779, 2022.
- [17] Yanfeng Ge, Zhicui Wang, Xing Wang, Wenhui Wan, and Yong Liu. Superconductivity in the two-dimensional nonbenzenoid biphenylene sheet with dirac cone. *2D Materials*, 9(1):015035, 2021.
- [18] R. W. Godby and R. J. Needs. Metal-insulator transition in kohn-sham theory and quasiparticle theory. *Phys. Rev. Lett.*, 62:1169–1172, Mar 1989.
- [19] C. Godet and M.N. Berberan-Santos. Evidence for excitonic behavior of photoluminescence in polymer-like a-c:h films. *Diamond and Related Materials*, 10(2):168–173, 2001. Proceedings of the 3rd Specialist Meeting on Amorphous Carbon.
- [20] Taylan Gorkan, Salih Demirci, Johannes V. Barth, Ethem Aktürk, and Salim Ciraci. Can stable mos2 monolayers and multilayers be constituted in the biphenylene network? *The Journal of Physical Chemistry C*, 127(18):8770–8777, May 2023.
- [21] G. N. Greaves, A. L. Greer, R. S. Lakes, and T. Rouxel. Poisson’s ratio and modern materials. *Nature Materials*, 10(11):823–837, Nov 2011.
- [22] Stefan Grimme, Jens Antony, Stephan Ehrlich, and Helge Krieg. A consistent and accurate ab initio parametrization of density functional dispersion correction (DFT-D) for the 94 elements H-Pu. *The Journal of Chemical Physics*, 132(15):154104, 04 2010.
- [23] Stefan Grimme, Stephan Ehrlich, and Lars Goerigk. Effect of the damping function in dispersion corrected density functional theory. *Journal of Computational Chemistry*, 32(7):1456–1465, 2011.
- [24] Ting Han, Yu Liu, Xiaodong Lv, and Fengyu Li. Biphenylene monolayer: a novel nonbenzenoid

- carbon allotrope with potential application as an anode material for high-performance sodium-ion batteries. *Phys. Chem. Chem. Phys.*, 24:10712–10716, 2022.
- [25] Q. Hassanzada, I. Abdolhosseini Sarsari, A. Hashemi, A. Ghojavand, A. Gali, and M. Abdi. Theoretical study of quantum emitters in two-dimensional silicon carbide monolayers. *Phys. Rev. B*, 102:134103, Oct 2020.
- [26] Jochen Heyd and Gustavo E. Scuseria. Efficient hybrid density functional calculations in solids: Assessment of the Heyd–Scuseria–Ernzerhof screened Coulomb hybrid functional. *The Journal of Chemical Physics*, 121(3):1187–1192, 07 2004.
- [27] Jochen Heyd, Gustavo E. Scuseria, and Matthias Ernzerhof. Hybrid functionals based on a screened Coulomb potential. *The Journal of Chemical Physics*, 118(18):8207–8215, 05 2003.
- [28] Jochen Heyd, Gustavo E. Scuseria, and Matthias Ernzerhof. Erratum: “Hybrid functionals based on a screened Coulomb potential” [J. Chem. Phys. 118, 8207 (2003)]. *The Journal of Chemical Physics*, 124(21):219906, 06 2006.
- [29] Roald Hoffmann, Artyom A. Kabanov, Andrey A. Golov, and Davide M. Proserpio. Homocitans and carbon allotropes: For an ethics of citation. *Angewandte Chemie International Edition*, 55(37):10962–10976, 2016.
- [30] H. C. Hsueh, G. Y. Guo, and Steven G. Louie. Excitonic effects in the optical properties of a sic sheet and nanotubes. *Phys. Rev. B*, 84:085404, Aug 2011.
- [31] Mathew A. Hudspeth, Brandon W. Whitman, Veronica Barone, and Juan E. Peralta. Electronic properties of the biphenylene sheet and its one-dimensional derivatives. *ACS Nano*, 4(8):4565–4570, Aug 2010.
- [32] H. Şahin, S. Cahangirov, M. Topsakal, E. Bekaroglu, E. Akturk, R. T. Senger, and S. Ciraci. Monolayer honeycomb structures of group-iv elements and iii-v binary compounds: First-principles calculations. *Phys. Rev. B*, 80:155453, Oct 2009.
- [33] Jiří Klimeš, David R. Bowler, and Angelos Michaelides. Van der waals density functionals applied to solids. *Phys. Rev. B*, 83:195131, May 2011.
- [34] Jiří Klimeš, David R Bowler, and Angelos Michaelides. Chemical accuracy for the van der waals density functional. *Journal of Physics: Condensed Matter*, 22(2):022201, dec 2009.
- [35] G. Kresse and J. Furthmüller. Efficient iterative schemes for ab initio total-energy calculations using a plane-wave basis set. *Phys. Rev. B*, 54:11169–11186, Oct 1996.
- [36] G. Kresse and J. Furthmüller. Efficiency of ab-initio total energy calculations for metals and

- semiconductors using a plane-wave basis set. *Computational Materials Science*, 6(1):15–50, 1996.
- [37] G. Kresse and D. Joubert. From ultrasoft pseudopotentials to the projector augmented-wave method. *Phys. Rev. B*, 59:1758–1775, Jan 1999.
- [38] H. W. Kroto, J. R. Heath, S. C. O’Brien, R. F. Curl, and R. E. Smalley. C60: Buckminsterfullerene. *Nature*, 318(6042):162–163, Nov 1985.
- [39] Aliaksandr V. Krukau, Oleg A. Vydrov, Artur F. Izmaylov, and Gustavo E. Scuseria. Influence of the exchange screening parameter on the performance of screened hybrid functionals. *The Journal of Chemical Physics*, 125(22):224106, 12 2006.
- [40] Stephan Kümmel and Leeor Kronik. Orbital-dependent density functionals: Theory and applications. *Rev. Mod. Phys.*, 80:3–60, Jan 2008.
- [41] Manuel Längle, Kenichiro Mizohata, Clemens Mangler, Alberto Trentino, Kimmo Mustonen, E Harriet Åhlgren, and Jani Kotakoski. Two-dimensional few-atom noble gas clusters in a graphene sandwich. *Nature Materials*, pages 1–6, 2024.
- [42] H. M. Lawler, J. J. Rehr, F. Vila, S. D. Dalosto, E. L. Shirley, and Z. H. Levine. Optical to uv spectra and birefringence of  $\text{SiO}_2$  and  $\text{TiO}_2$ : First-principles calculations with excitonic effects. *Phys. Rev. B*, 78:205108, Nov 2008.
- [43] Tue Minh Le Nguyen, Vo Van Hoang, and Hang T. T. Nguyen. Structural evolution of free-standing 2d silicon carbide upon heating. *The European Physical Journal D*, 74(6):108, Jun 2020.
- [44] Guoxing Li, Yuliang Li, Huibiao Liu, Yanbing Guo, Yongjun Li, and Daoben Zhu. Architecture of graphdiyne nanoscale films. *Chemical Communications*, 46(19):3256–3258, 2010.
- [45] Linyang Li, Xiangru Kong, and François M Peeters. New nanoporous graphyne monolayer as nodal line semimetal: Double dirac points with an ultrahigh fermi velocity. *Carbon*, 141:712–718, 2019.
- [46] Xiaoyin Li, Qian Wang, and Puru Jena.  $\psi$ -graphene: a new metallic allotrope of planar carbon with potential applications as anode materials for lithium-ion batteries. *The journal of physical chemistry letters*, 8(14):3234–3241, 2017.
- [47] Yingjie Li, Yangyang Li, Peng Lin, Jing Gu, Xiaojun He, Moxin Yu, Xiaoting Wang, Chuan Liu, and Chunxi Li. Architecture and electrochemical performance of alkynyl-linked naphthyl carbon skeleton: Naphyne. *ACS applied materials & interfaces*, 12(29):33076–33082, 2020.



- [48] S. S. Lin. Light-emitting two-dimensional ultrathin silicon carbide. *The Journal of Physical Chemistry C*, 116(6):3951–3955, Feb 2012.
- [49] Yung-Chang Lin, Rika Matsumoto, Qiunan Liu, Pablo Solís-Fernández, Ming-Deng Siao, Po-Wen Chiu, Hiroki Ago, and Kazu Suenaga. Alkali metal bilayer intercalation in graphene. *Nature communications*, 15(1):425, 2024.
- [50] Qihang Liu and Alex Zunger. Predicted realization of cubic dirac fermion in quasi-one-dimensional transition-metal monochalcogenides. *Phys. Rev. X*, 7:021019, May 2017.
- [51] Tianyang Liu, Yu Jing, and Yafei Li. Two-dimensional biphenylene: A graphene allotrope with superior activity toward electrochemical oxygen reduction reaction. *The Journal of Physical Chemistry Letters*, 12(51):12230–12234, Dec 2021.
- [52] Hui Long, Jianwei Hu, Xing Xie, Peiju Hu, Shaoxiong Wang, Minru Wen, Xin Zhang, Fugen Wu, and Huafeng Dong. Sic siligraphene: a novel sic allotrope with wide tunable direct band gap and strong anisotropy. *Journal of Physics D: Applied Physics*, 54(22):225102, mar 2021.
- [53] Johann Lüder, Monica de Simone, Roberta Totani, Marcello Coreno, Cesare Grazioli, Biplab Sanyal, Olle Eriksson, Barbara Brena, and Carla Puglia. The electronic characterization of biphenylene—experimental and theoretical insights from core and valence level spectroscopy. *The Journal of chemical physics*, 142(7), 2015.
- [54] Yi Luo, Yiqiang He, Yunfei Ding, Lijie Zuo, Chengyong Zhong, Yinchang Ma, and Minglei Sun. Defective biphenylene as high-efficiency hydrogen evolution catalysts. *Inorganic Chemistry*, 63(2):1136–1141, Jan 2024.
- [55] Yi Luo, Chongdan Ren, Yujing Xu, Jin Yu, Sake Wang, and Minglei Sun. A first principles investigation on the structural, mechanical, electronic, and catalytic properties of biphenylene. *Scientific reports*, 11(1):19008, 2021.
- [56] Nicola Marzari, Arash A. Mostofi, Jonathan R. Yates, Ivo Souza, and David Vanderbilt. Maximally localized wannier functions: Theory and applications. *Rev. Mod. Phys.*, 84:1419–1475, Oct 2012.
- [57] Mohammad Ali Mohebpour, Shobair Mohammadi Mozvashi, Sahar Izadi Vishkayi, and Meysam Bagheri Tagani. Transition from metal to semiconductor by semi-hydrogenation of borophene. *Phys. Rev. Mater.*, 6:014012, Jan 2022.
- [58] Hendrik J. Monkhorst and James D. Pack. Special points for brillouin-zone integrations. *Phys. Rev. B*, 13:5188–5192, Jun 1976.

- [59] E. Mostaani, N. D. Drummond, and V. I. Fal'ko. Quantum monte carlo calculation of the binding energy of bilayer graphene. *Phys. Rev. Lett.*, 115:115501, Sep 2015.
- [60] Arash A. Mostofi, Jonathan R. Yates, Giovanni Pizzi, Young-Su Lee, Ivo Souza, David Vanderbilt, and Nicola Marzari. An updated version of wannier90: A tool for obtaining maximally-localised wannier functions. *Computer Physics Communications*, 185(8):2309–2310, 2014.
- [61] Nicolas Mounet and Nicola Marzari. First-principles determination of the structural, vibrational and thermodynamic properties of diamond, graphite, and derivatives. *Phys. Rev. B*, 71:205214, May 2005.
- [62] Shūichi Nosé. A molecular dynamics method for simulations in the canonical ensemble. *Molecular physics*, 52(2):255–268, 1984.
- [63] Shuichi Nosé. A unified formulation of the constant temperature molecular dynamics methods. *The Journal of Chemical Physics*, 81(1):511–519, 07 1984.
- [64] K. S. Novoselov, A. K. Geim, S. V. Morozov, D. Jiang, Y. Zhang, S. V. Dubonos, I. V. Grigorieva, and A. A. Firsov. Electric field effect in atomically thin carbon films. *Science*, 306(5696):666–669, 2004.
- [65] Giovanni Onida, Lucia Reining, and Angel Rubio. Electronic excitations: density-functional versus many-body green's-function approaches. *Rev. Mod. Phys.*, 74:601–659, Jun 2002.
- [66] Qingyan Pan, Siqi Chen, Chenyu Wu, Feng Shao, Jing Sun, Lishui Sun, Zhaohui Zhang, Yixiao Man, Zhibo Li, Lixia He, et al. Direct synthesis of crystalline graphtetrayne—a new graphyne allotrope. *CCS Chemistry*, 3(4):1368–1375, 2021.
- [67] John P. Perdew, Kieron Burke, and Matthias Ernzerhof. Generalized gradient approximation made simple. *Phys. Rev. Lett.*, 77:3865–3868, Oct 1996.
- [68] M. L. Pereira, W. F. da Cunha, R. T. de Sousa, G. D. Amvame Nze, D. S. Galvão, and L. A. Ribeiro. On the mechanical properties and fracture patterns of the nonbenzenoid carbon allotrope (biphenylene network): a reactive molecular dynamics study. *Nanoscale*, 14:3200–3211, 2022.
- [69] C. M. Polley, H. Fedderwitz, T. Balasubramanian, A. A. Zakharov, R. Yakimova, O. Bäcke, J. Ekman, S. P. Dash, S. Kubatkin, and S. Lara-Avila. Bottom-up growth of monolayer honeycomb sic. *Phys. Rev. Lett.*, 130:076203, Feb 2023.
- [70] Michael Rohlfing and Steven G. Louie. Electron-hole excitations and optical spectra from first principles. *Phys. Rev. B*, 62:4927–4944, Aug 2000.

- [71] Masoud Shahrokhi. Quasi-particle energies and optical excitations of zns monolayer honeycomb structure. *Applied Surface Science*, 390:377–384, 2016.
- [72] Masoud Shahrokhi and Céline Leonard. Tuning the band gap and optical spectra of silicon-doped graphene: Many-body effects and excitonic states. *Journal of Alloys and Compounds*, 693:1185–1196, 2017.
- [73] Babu Ram Sharma, Aaditya Manjanath, and Abhishek K Singh. pentahexoctite: A new two-dimensional allotrope of carbon. *Scientific reports*, 4(1):7164, 2014.
- [74] Arushi Singh, Vikram Mahamiya, and Alok Shukla. Defect-driven tunable electronic and optical properties of two-dimensional silicon carbide. *Phys. Rev. B*, 108:235311, Dec 2023.
- [75] Qi Song, Bing Wang, Ke Deng, Xinliang Feng, Manfred Wagner, Julian D Gale, Klaus Müllen, and Linjie Zhi. Graphenylene, a unique two-dimensional carbon network with nondelocalized cyclohexatriene units. *Journal of Materials Chemistry C*, 1(1):38–41, 2013.
- [76] G. Strinati. Application of the green’s functions method to the study of the optical properties of semiconductors. *La Rivista del Nuovo Cimento (1978-1999)*, 11(12):1–86, Dec 1988.
- [77] Toma Susi, Viera Skákalová, Andreas Mittelberger, Peter Kotrusz, Martin Hulman, Timothy J. Pennycook, Clemens Mangler, Jani Kotakoski, and Jannik C. Meyer. Computational insights and the observation of sic nanograin assembly: towards 2d silicon carbide. *Scientific Reports*, 7(1):4399, Jun 2017.
- [78] Meysam Bagheri Tagani. si<sub>9</sub>c<sub>15</sub> monolayer: A silicon carbide allotrope with remarkable physical properties. *Phys. Rev. B*, 107:085114, Feb 2023.
- [79] H. Terrones, M. Terrones, E. Hernández, N. Grobert, J-C. Charlier, and P. M. Ajayan. New metallic allotropes of planar and tubular carbon. *Phys. Rev. Lett.*, 84:1716–1719, Feb 2000.
- [80] Atsushi Togo, Laurent Chaput, Terumasa Tadano, and Isao Tanaka. Implementation strategies in phonopy and phono3py. *Journal of Physics: Condensed Matter*, 35(35):353001, jun 2023.
- [81] Raphael M. Tromer, Marcelo L. Pereira Júnior, Kleuton A. L. Lima, Alexandre F. Fonseca, Luciano R. da Silva, Douglas S. Galvão, and Luiz. A. Ribeiro Junior. Mechanical, electronic, and optical properties of 8-16-4 graphyne: A 2d carbon allotrope with dirac cones. *The Journal of Physical Chemistry C*, 127(25):12226–12234, Jun 2023.
- [82] Vo Van Hoang, Nguyen Hoang Giang, To Quy Dong, and Tran Thi Thu Hanh. Tetra-sic – new allotrope of 2d silicon carbide. *Computational Materials Science*, 162:236–244, 2019.
- [83] Harish P. Veeravenkata and Ankit Jain. Density functional theory driven phononic thermal

- conductivity prediction of biphenylene: A comparison with graphene. *Carbon*, 183:893–898, 2021.
- [84] Zhenhai Wang, Xiang-Feng Zhou, Xiaoming Zhang, Qiang Zhu, Huafeng Dong, Mingwen Zhao, and Artem R Oganov. Phagraphene: a low-energy graphene allotrope composed of 5–6–7 carbon rings with distorted dirac cones. *Nano letters*, 15(9):6182–6186, 2015.
- [85] Qun Wei, Ying Yang, Guang Yang, and Xihong Peng. New stable two dimensional silicon carbide nanosheets. *Journal of Alloys and Compounds*, 868:159201, 2021.
- [86] Li Yang, Jack Deslippe, Cheol-Hwan Park, Marvin L. Cohen, and Steven G. Louie. Excitonic effects on the optical response of graphene and bilayer graphene. *Phys. Rev. Lett.*, 103:186802, Oct 2009.
- [87] Pei Zhang, Tao Ouyang, Chao Tang, Chaoyu He, Jin Li, Chunxiao Zhang, Ming Hu, and Jianxin Zhong. The intrinsic thermal transport properties of the biphenylene network and the influence of hydrogenation: a first-principles study. *J. Mater. Chem. C*, 9:16945–16951, 2021.
- [88] Wei Zhang, Changchun Chai, Qingyang Fan, Yanxing Song, Yuqian Liu, Yintang Yang, Minglei Sun, and Udo Schwingenschlogl. Semimetallic 2d alkynyl carbon materials with distorted type i dirac cones. *The Journal of Physical Chemistry C*, 125(32):18022–18030, 2021.
- [89] Liujiang Zhou, Huilong Dong, and Sergei Tretiak. Recent advances of novel ultrathin two-dimensional silicon carbides from a theoretical perspective. *Nanoscale*, 12:4269–4282, 2020.